PRINTED & MUSCULOSKELETAL ROBOTICS

A forward-engineered, muscle-driven soft robotic swimmer

William Cartwright Drennan[1,2]*, Onur Aydin[1,2,3], Bashar Emon[1,2], Zhengwei Li[4], Md Saddam Hossain Joy[1,2], Alexandra Barishman[5], Yelim Kim[1,6], Margaret Wei[5], Danette Denham[7], Annika Carrillo[5], M. Taher A. Saif[1,2]*

The field of biohybrid robotics focuses on using biological actuators to study the emergent properties of tissues and the locomotion of living organisms. On the basis of models of swimming at small size scales, we designed and fabricated a muscle-powered, flagellate swimmer. We investigate the design of a compliant mechanism based on nonlinear mechanics and its mechanical integration with a muscle ring and motor neurons. We find that within a range of anchor stiffnesses around 1 micronewton per micrometer, the homeostatic tension in muscle is insensitive to stiffness, offering greater design flexibility. The proximity of motor neurons results in a fourfold improvement in muscle contractility. Improved contractility and nonlinear design allow for a peak swimming speed about two orders of magnitude higher than previous biohybrid flagellate swimmers, reaching 0.58 body lengths per minute (86.8 micrometers per second), by a mechanism involving inertia that we verify through flow field imaging. This swimmer opens the door for a class of intermediate–Reynolds number swimmers.

INTRODUCTION

Biohybrid robots have emerged over the past two decades as platforms to study the biomechanics of living actuators as well as novel fabrication and control techniques (*1*–*5*). They usually consist of cardiac or skeletal muscle interfaced with a soft scaffold (silicone elastomers and hydrogels) and either operate autonomously or receive pacing through electrical or optogenetic stimulation. Key advantages of muscle over conventional actuators are its abilities to grow in situ at small scales and to follow external pacing. Several recently developed muscle-actuated robots, ranging in size scale from 10^{-4} to 10^{-2} m, have allowed for the basic study of small-scale locomotion and emergent behaviors of biological tissues (*6*–*8*). They include biomimetic swimmers resembling jellyfish (*9*, *10*), manta rays (*11*), and flagellates (*12*, *13*), crawling robots that use structural asymmetry to achieve unidirectional motion (*14*–*16*), a valveless pumping robot (*17*), and a variety of micromanipulators which function both in (*18*) and out (*19*, *20*) of medium. The swimming ability of microbial flagellates is of particular interest because of their simple body plan and suitability for theoretical study.

Flagellate swimmers generate thrust by moving their flagella in a planar rowing or three-dimensional (3D) corkscrew motion. These wave-like motions fulfill a requirement for net propulsion at the size scales and speeds relevant to microbes. We can describe the flow around these microbes with a Reynolds number (*Re*), which is a dimensionless parameter describing the relative contributions of inertia and viscous drag. Microbes moving their flagella provide boundary conditions to the surrounding fluid. In addition, in the limit of a vanishing *Re*, the motion in the fluid is dominated by viscous drag. These are called creeping flows, and the regime is called Stokes flow. In this limit, swimming becomes possible only through nonreciprocal, time-asymmetric body motions, such as a wave. This is known as scallop theorem (*21*), and it arises because in the limit of vanishing *Re*, a flow subjected to forces from a swimming body reaches mechanical equilibrium instantaneously (*22*). A consequence of this is that a given sequence of body motions will result in the same change in position regardless of how quickly the body motions are executed. For a human, this type of swimming would only be accessible through slow movements (1 mm/s) in an extremely viscous fluid, such as molasses where $Re \sim 10^{-2}$ (*23*). Flagellate swimmers naturally operate across a range of low *Re*. They include some types of bacteria and algae operating at $Re \sim 10^{-6}$ and sperm gametes operating in the range of $Re \sim 10^{-5}$ to 10^{-2} (*24*–*28*). At these low *Re* values, we can model their swimming behavior with linear models of Stokes flow and linear models of their flagella dynamics.

Fabricating a low-*Re* flagellate requires a small and controllable actuator, for which biological muscle is well suited. Studies looking to control muscle-powered actuators have pursued the emergent integration of neural tissues with skeletal muscle, using cerebral (*29*), cortical (*30*), and motor neurons (*12*, *31*–*35*). A recently developed flagellate-like biohybrid swimmer demonstrated the formation of an untethered, neuromuscular actuator through the emergence of neuromuscular junctions (NMJs) between a skeletal muscle strip and optogenetic motor neurons (*12*). The optically excitable neuromuscular actuator was used to pull on a pair of thin tails, eliciting a time-asymmetric waving motion that produced net thrust at low *Re* ($\sim 10^{-3}$). This swimmer achieved a top speed of 0.7 μm/s or 0.014 body lengths/min, much slower than natural flagellate swimmers, such as sperm that swim on the order of 100 body lengths/min (*24*).

Other small-scale biohybrid swimmers, including a serpentine spring–shaped swimmer (*8*) and a cardiac muscle–powered biohybrid ray ($Re \sim 10^{1}$) (*11*), have been shown to reach relative average velocities of 2.77 and 6.42 body lengths/min, respectively, where the mechanism of thrust generation is different from flagellum-mediated swimming. The biohybrid ray generates thrust through nonreciprocal

---

[1]Department of Mechanical Science and Engineering, University of Illinois at Urbana-Champaign, Urbana, IL, USA. [2]CZ Biohub Chicago LLC, Chicago, IL, USA. [3]Carl R. Woese Institute for Genomic Biology, University of Illinois at Urbana-Champaign, Urbana, IL, USA. [4]Cullen College of Engineering, Biomedical Engineering, University of Houston, Houston, TX, USA. [5]Department of Bioengineering, University of Illinois at Urbana-Champaign, Urbana, IL, USA. [6]School of Education and Social Policy, Northwestern University, Evanston, IL, USA. [7]Department of Molecular and Cellular Biology, University of Illinois Urbana-Champaign, Urbana, IL, USA.
*Corresponding author. Email: wcd2@illinois.edu (W.C.D.); saif@illinois.edu (M.T.A.S.)

waves propagating along its elastomeric body generated by a propagation delay in a network of contracting cardiac cells. These waves would likewise generate net thrust at low *Re*. We expect a change in how thrust is generated by a given nonreciprocal motion as we transition from a low-*Re* regime to a high-*Re* regime. Researchers have investigated this transition theoretically for a few special cases including a swimmer that is much denser than the surrounding fluid and for a swimmer near a boundary, but the general case of a swimmer with density similar to the fluid has not been addressed (*36*, *37*).

Here, we explore the design space for a flagellate-type biohybrid swimmer and demonstrate a prototype with high swimming performance. The mechanical design elements are developed on the basis of the theory of the hydrodynamics of flagellates and large-deflection analysis of compliant mechanisms. In developing the biological elements, we consider skeletal muscle contraction dynamics, muscle-neuron interactions, and the roles of scaffold mechanics on muscle development and maturation.

Simulations based on the theory of flagellate-swimming suggest that propulsion can be substantially increased by adjusting the boundary conditions at the base of the flagella. In the basic body plan of a biohybrid flagellate, muscle contractions induce translational and angular displacements at the ends of a pair of thin tails. The tails respond similar to Euler-Bernoulli beams with boundary conditions from the muscle and body forces from the resistance of the fluid. From the reaction forces on the tail by the fluid, the net propulsion force is calculated (*12*, *38*). Hydrodynamics simulations have shown that propulsion force is strongly dependent on the amplitude of the angular displacement boundary condition in particular (*39*). To take advantage of this dependency, one can design a compliant mechanism that transforms the displacements generated by muscle contraction into large angular deflections. Designing a mechanical element that undergoes large deflection introduces an additional challenge. The small angle assumption ($dy/dx \ll 1$) that is used to derive solutions to the linearized Euler-Bernoulli beam equation will be invalid, and geometric nonlinearities will need to be accounted for (*40*). Theoretical analysis of a compliant hinge mechanism for large-angle biohybrid actuation has been presented previously (*39*). Here, we demonstrate the fabrication, characterization, and testing of this compliant mechanism as a mechanical element integrated into a bioactuator design.

In a biohybrid system, the mechanical and biological design elements are naturally interlinked. To achieve functional muscle fibers that provide a robust source of actuation, it is necessary to ensure that the mechanical elements support proper development and maturation of the muscle. The process by which muscle fibers mature, termed myofibrillogenesis, depends on several mechanical and chemical factors (*41*).

Mechanical factors

During the maturation process, myoblasts (muscle progenitor cells) fuse into multinucleated nascent myotubes that stretch out and pull on the surrounding matrix. On the basis of in vivo studies of *Drosophila* abdominal muscles, this pulling generates tension and is necessary for the formation of immature contractile units of actin and myosin (*42*). These immature units undergo spontaneous, calcium-dependent twitching, which appears to be necessary for the organization of highly periodic cross-striated sarcomeres, the key force generating units in skeletal muscle. For maturation to occur, the attachments of a muscle need to be stiff enough to allow tension to develop and yet compliant enough to allow the muscle to twitch. The effect of tuning mechanical stiffness on muscle tissue compaction has been explored on-board a biohybrid swimmer with mechanical stiffness between 0.4 and 3 μN/μm. The soft muscle scaffolds allow for auxotonic spontaneous twitching where the scaffold provides mechanical feedback. Their results show tissue shortening during maturation inversely proportional to stiffness and improved force generation for a scaffold with overall stiffness of 0.5 μN/μm compared to stiffer pillar structures (*8*). Another study on muscle strip differentiation around soft pillar structures found an optimal mechanical stiffness of 2 μN/μm for muscle differentiation (*31*).

Chemical factors

In vitro studies with the immortalized mouse myoblasts cell line C2C12 often use serum concentration to shift the cells from a proliferative state toward differentiation. This involves exchanging 10% (v/v) fetal bovine serum for 2 to 10% (v/v) horse serum with additional growth factor supplements such as insulin-transferrin-selenium (ITS) (*43*, *44*). A remarkable finding from in vitro studies of NMJ formation is that the spontaneous twitching of C2C12-derived skeletal muscle increases in the presence of motor neurons (*30*, *31*). One study working with C2C12-derived muscle tissues in the presence of mouse embryonic stem cell (mESC)–derived motor neurons observed preferential outgrowth of neurites toward the muscle, higher spontaneous contractility, and a 60% higher ratio of cross-striated myofibers to immature myotubes in cocultured samples (*31*). Another study developed a system for culturing cortical, spinal, and muscle organoids together (*30*). Significantly more spontaneous twitching events were observed in the muscle in the presence of the spinal organoid, although the sample-to-sample variability was high. Transmission electron microscopy images of the multiorganoid samples showed highly organized, cross-striated sarcomeres, which is evidence of maturity. We therefore expect that neurons in the vicinity of a muscle culture will improve muscle maturation as demonstrated by an increase in overall contractility.

In the following section, we present our design and analysis of a fast, muscle-powered, biohybrid flagellate–type swimmer based on low-*Re* theory. After discussing the mechanical and biological design elements, we present calibration and characterization of these elements looking at how tissue-scaffold and muscle-neuron interactions affect the performance of the muscle. We seek to answer several questions including (i) what challenges exist in designing and interfacing a micromolded compliant mechanism with muscle, (ii) how variable and time-dependent mechanical stiffness affects the tonic tension that the muscle develops during maturation, (iii) how the proximity of motor neurons affects muscle performance, (iv) whether increasing tail angular actuation results in swimming velocities that agree with predictions of low-*Re* simulations, and (v) whether this results in improved swimming speed. Concerning the design of a compliant muscle-driven mechanism (i), we find challenges with unintended modes of compliance hindering efficient conversion of muscle contraction into angular displacement. Concerning muscle maturation (ii), we find that it is invariant to the history of mechanical stiffness. Rather, the muscle tends toward a time-varying, homeostatic tension, which is robust to perturbation in stiffness. This observation has implications for understanding the mechanosensitivity of muscle development and the role of tonic tension during myogenesis. Future biohybrid platforms may exploit this robustness to their design advantage. Concerning the effect of the proximity of motor neurons (iii), we find an improvement in muscle contractility within 2 days of adding motor neurons, before we expect to see functional innervation. We propose that this has implications for the role of neuron-muscle coculture on the timeline of myogenesis. Last, concerning swimming performance (iv and v), we find that our experimental swimming speeds far exceed predictions from low-*Re* simulations using the same muscle actuation observed in our experiments. Rather, we see that above a threshold angular displacement of the tails, there is a sharp increase in swimming velocity. Using particle streak imaging and a programmable micromanipulator, we explore the flow field around a fixed swimmer scaffold and observe a transition in the flow dynamics with inertial effects that depend both on tail angular displacement and the actuation velocity. In the discussion, we consider this transition with respect to the theoretical and experimental literature on the transition in swimming dynamics between a low-*Re* $O(10^{-4})$ and an intermediate-*Re* $O(1)$ flow regime.

RESULTS

Biohybrid swimmer design

Overall concept

We design a swimmer based around a compliant mechanism that converts muscle contraction into large amplitude angular displacements of a pair of thin tails to generate thrust (Fig. 1A). Compliance of the muscle anchors permits spontaneous twitching that has been shown to aid in muscle development. We introduce motor neurons into the swimmer to support the maturation of the muscle. Over 10 to 13 days, the muscle develops tonic force, pulling on the compliant mechanisms and moving the swimmer tails closer to the center of the swimmer. When electrical stimulation is applied, the angular displacement of the tails produces thrust moving the swimmer forward.

Overall, the swimmer consists of a soft, polydimethylsiloxane (PDMS) scaffold composed of a bulbous head and a pair of thin tails, a ring of skeletal muscle made from C2C12 mouse myoblasts, and a cluster of mESC-derived motor neurons (Fig. 1D). In the following sections, we go into the design considerations of each of these elements.

Swimmer tails

The swimmer tails attach to the head of the swimmer via a compliant mechanism that transforms the muscle contraction into angular displacement. For a 4-mm-long muscle that shortens by 4% of its resting length during electrical stimulation (*12*), the absolute displacement for each grip anchoring the muscle would be 80 μm. This is the baseline for the actuation input we use to evaluate our design. This displacement of the grips δ_g is converted by the compliant mechanism into translational displacement δ and angular displacement $\Delta\theta$ of the base of the tails (Fig. 1E). The dynamics of the tails in response to this actuation generates net time-averaged thrust $(\langle F_{\text{prop}} \rangle)$ for the swimmer in the forward direction. The components of thrust of the tails normal to the direction of swimming cancel with one another. At low *Re*, the time-averaged velocity of the swimmer, denoted by $\langle v \rangle$, is the time average of the thrust divided by the total drag on the untethered system γ, given by $\langle v \rangle = \langle F_{\text{prop}} \rangle / \gamma$. In the limit of vanishing *Re* and for an arbitrarily slender tail, there exists an asymmetry between the drag per unit length along the tail $\zeta_{\parallel}$ and perpendicular to the tail $\zeta_{\perp}$. Net thrust generation depends on this asymmetry, such that $F_{\text{prop}} \propto (\zeta_{\perp} - \zeta_{\parallel})$ (*38*). From resistive force theory we have that in the limit of the ratio of the length of the filament L to the radius of the filament r, $L/r \to \infty$, the perpendicular and parallel drag coefficients are related by $\zeta_{\perp} = 2\zeta_{\parallel}$ (*45*). In our design $L/r \approx 90$, so we expect $\zeta_{\perp} = 1.6\zeta_{\parallel}$ (*39*). Because $\zeta_{\parallel}$ is less than $\zeta_{\perp}$, the tails contribute the least drag to the overall system when their resting configuration orients along the direction of swimming. During development, the muscle generates tonic tension, pulling the tails toward the middle of the swimmer. To compensate for this, we initially orient the tails 60° away from the muscle. When the tails are oriented along the direction of swimming, they contribute drag to the system $\gamma_{\text{tails}} = 2L\zeta_{\parallel}$.

For a fixed actuation amplitude and tail cross section that determines the drag coefficients, the thrust generated by the tails is fully

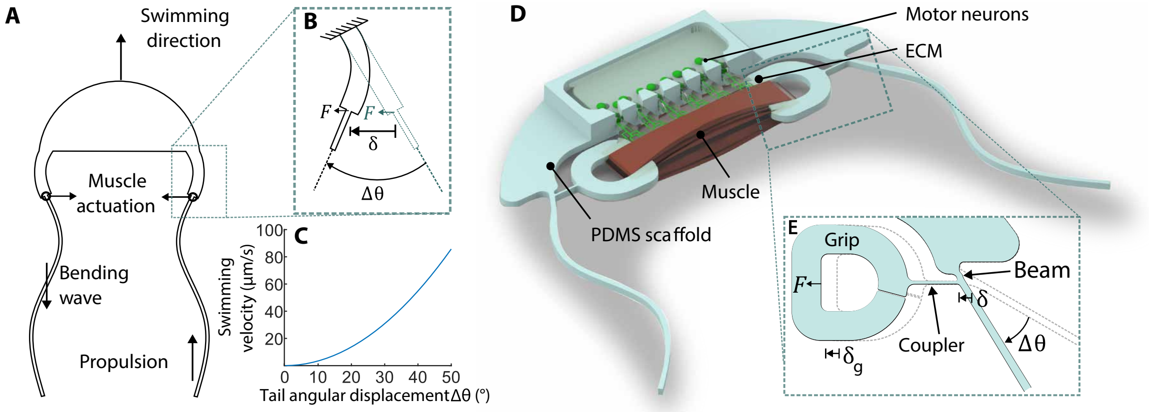

Fig. 1. Design for the biohybrid swimmer. The amount of curvature in the swimmer tails is exaggerated in these images to convey the idea of a propagating wave. The optimal swimming speed for a low-*Re* swimmer occurs when the amount of curvature in the tail is approximately one-quarter of a full wave. (**A**) Conceptual design highlighting the role of large angular displacement of the base of the tails for generating large amplitude bending waves and propulsion. The relationship between swimming velocity and tail angle change is derived from numerical simulations of the elastohydrodynamic model of the swimmer. (**B**) A conceptual compliant hinge mechanism, whereby the motion of a muscle contracting and relaxing by distance δ creates an angular displacement $\Delta\theta$ at the base of the tail. (**C**) Simulated relationship between the angular displacement of the tail and the swimming velocity. (**D**) Rendering of the biohybrid implementation of the conceptual design. (**E**) The micromolded PDMS realization of the compliant tail mechanism.

determined by their sperm number, Sp, which is a dimensionless parameter that comes from nondimensionalizing the equations governing the system while assuming periodic boundary conditions with angular frequency ω (*38*), which is taken to be the frequency of muscle contraction. The value of Sp depends on the length of the tail L, on the actuation frequency ω, and on the flexural rigidity A, and it is given by $Sp = L\left(\frac{\omega\xi_\perp}{A}\right)^{1/4}$. For low-*Re* swimmers, thrust is negligible for $Sp < 1$ and is at a maximum around an Sp of 2.1 (*38*). Our design uses an intermediate value with an Sp of 1.4 (see Materials and Methods).

Compliant mechanism

A compliant mechanism connects the muscle to the tails (Fig. 1E). We can frame this mechanism as a compliant slider-crank linkage. The muscle attaches to the mechanism by wrapping around a grip, acting as the slider that drives the linkage. A thin coupler connects the grip to the end of a compliant beam that acts as the crank. A compliant beam undergoing large angular deflection acts similar to a hinge, producing larger angular displacement than its rigid counterpart for the same input displacement (Fig. 1B) (*39*). The swimmer tail is attached at the end of this beam, and so the translation and angular deflection of this beam provide the boundary conditions δ and $\Delta\theta$ for the swimmer tails (Fig. 1, B and E). The reactionary moment of the coupler on the tip of the beam will act to reduce the angular deflection. Because our low-*Re* theory predicts higher swimming velocities for larger angular deflection (Fig. 1C), we try to reduce this moment by making the point of attachment between the coupler and the beam as small as possible. This also means that the attachment between the grip and the rest of the scaffold will be floppy. To facilitate muscle attachment, whether by in situ formation or by mounting a ring of muscle onto the scaffold, there needs to be sacrificial supports that support the grips and attach them to the swimmer head.

Swimmer head

The swimmer head provides a point of attachment for the compliant tail mechanism, the sacrificial supports for the muscle grips, and the holder for motor neurons. At the start of fabrication, thin supports connect the muscle grips to the swimmer head directly. These supports are intended to be cut once the muscle is mounted, allowing it to pull directly on the tails. The width of the head contributes to the swimmer drag, limits the size of a muscle that can be attached to the system, and affects the amount of hydrodynamic interaction between the tails. In our design (Fig. 1B), the head is 9 mm wide, which provides room for a 4-mm-long muscle tissue. We approximate the drag on the head (γ_{head}) to be that of a sphere at Stoke's flow with the same projected area in the direction of swimming. The Stokes drag on a sphere is given by the equation $\gamma_{\text{head}} = 6\pi\eta v r$, where η is the kinematic fluid viscosity, v is the velocity of the flow past the sphere, and r is the radius of the sphere. The head has a high aspect ratio (11:1) shape, and so the Stoke's drag on a finite cylinder, given by Lamb's solution, could give another approximation of the head drag. However, since this formula is dependent on velocity, we would not be able to report a single value for the head drag, and it would add nonlinearity to the numerical model of low-*Re* swimming (*46*). We therefore choose a sphere approximation. The overall drag of the swimmer scaffold is given by $\gamma = \gamma_{\text{head}} + \gamma_{\text{tails}}$.

Muscle tissue

Anchoring a muscle tissue to a synthetic scaffold requires some type of interface. This could be through a bioadhesive that allows muscle fibers and collagen to stick to the scaffold or through an indirect interface where the muscle wraps around the scaffold. A type of bioadhesive between PDMS and collagen-based tissues has been demonstrated for various cell types through treatment of the PDMS with oxygen plasma, followed by incubation in extracellular matrix (ECM) (*47*, *48*). This process, termed ECM adsorption, can create anchorage for the tissue. In our experience, this method is less reliable with muscle, and we observe the muscle tear itself off any attachment after a few days. In this study, we pursued an indirect interface by forming a muscle ring that will wrap around a pair of hook-shaped grips attached to the swimmer tails.

Muscle rings are grown from a mixture of ECM and myoblasts that undergo an emergent process of differentiation and maturation. The myoblasts collectively compact the matrix around a structure to form a ring (*17*, *31*, *49*). As the myoblasts compact the gel, they approach each other and fuse into multinucleated, nascent myotubes. Muscle rings can be formed and transferred onto the swimmer scaffold once they compact and before switching to differentiation medium. We found that rings with inner diameter greater than 3 mm could be manually transferred onto the swimmer scaffold consistently.

In our scaffold design, the grips are spaced 4 mm apart. For a scaffold thickness of 150 μm, a muscle ring with 3-mm inner diameter will be able to wrap around the grips with only 1.1 mm of slack, which gets taken up as the myoblasts continue to compact the ring and develop tonic tension. Having this slack aids with mounting, whereas too much slack will require more compaction by the tissue before it starts feeling the mechanical resistance of the scaffold.

Motor neurons

Evidence has been emerging that in vitro muscles mature better in coculture with motor neurons, potentially due to interaction mediated by mutual chemical cues (*30*, *31*, *50*, *51*). To improve the maturity of the muscle through motor neuron coculture, we dispense mESC-derived motor neurons on a PDMS holder affixed to the head of the swimmer. The holder keeps the motor neurons around 1 mm away from the muscle tissue to avoid any contact between neuron and muscle cell bodies. Studies have shown that spheroids of motor neurons in contact with skeletal muscle tissue form localized, functional NMJs (*32*, *52*), resulting in weak localized muscle activity. In contrast, neurons positioned away from the muscle formed NMJs and exhibited robust tissue-wide contraction (*31*, *53*). In our swimmer design, ECM is used to bridge the gap between the motor neuron spheroids and the muscle. Neurites extend through the ECM bridges toward the muscle, while the holder prevents the neuron spheroids from slipping onto the muscle during or after placement (Fig. 1B). When ECM is deposited around a muscle tissue, we observe that the muscle tissue pulls the ECM toward itself over several days. In addition, when motor neurons innervate muscle, they build up tension in their axons (*54*). Without mechanical anchorage, this force might pull the neurons toward the muscle.

Implementation and characterization

Scaffold fabrication and calibration

In fabricating and analyzing this design, we first consider the mechanical swimmer scaffold in isolation from the biological elements. The scaffold is molded in a polytetrafluoroethylene (PTFE)–coated, microfabricated silicon mold. The neuron holder is molded in a separate stereolithography (SLA) 3D-printed resin mold and is attached to the scaffold with liquid PDMS. For the purpose of analyzing its deformation response, the swimmer scaffold has been subdivided into four components: the grip, the coupler, the beam, and the head (Fig. 2A). We track the points labeled in the schematic Fig. 2A while pulling on the grip at x_4 with a known force. This way, we can track the effective stiffness of each of the components as a function of their elongation in the direction of pulling (Fig. 2B). Although this scheme does not account for the rotation of the grip as it opens or out-of-plane bending of the head, it can give us a sense for how the compliance of the individual components aids or hinders the swimmer's performance.

A tungsten wire affixed to a hypodermic needle and a three-axis micrometer stage applies a force to the scaffold grip. The tungsten wire is 5.7 mm long, with a circular cross-sectional diameter of 34 μm and a Young's modulus of 400 GPa (*55*). We use the formula for the stiffness of a fixed-free cantilever, $k = 3EI/L^3$, where E is Young's modulus, I is the second moment of area of the cross section, and L is the length of the tungsten needle. The deflection of the tungsten wire is measured with respect to the hypodermic needle as a reference (Fig. 2C). The assumed spring constant of the tungsten wire k_{tungsten} is 0.43 μN/μm, and we assume that it remains linear up to 25% of its length and a force of 610 μN. A beam undergoing large deflections stiffens as it bends. We can numerically solve the Euler-Bernoulli beam equation for large deflects and find that the tungsten wire stiffness would be 0.53 μN/μm at this large displacement, 23% greater than its initial stiffness (*39*, *40*). However, because the wire stiffness changes continuously, at a deflection of 25%, the force estimate from ignoring nonlinearity is off by only 8%. We therefore choose to treat the tungsten wire as having a constant linear spring stiffness up to deflections of 25% of its length. We calculate the force of the tungsten wire on the grip to be $F = k_{\text{tungsten}}\left(L_f - L_i\right)$, where L_i and L_f are the initial and instantaneous distance between the tungsten wire and the hypodermic needle, respectively. We define the stiffness of each of the elements (Fig. 2B) as the change in the applied force of the tungsten wire with respect to the change in their length in the direction of pulling.

Force-displacement curves are reported for each of the individual components (Fig. 2D). We see that each of these components contributes to the overall mechanical stiffness, with the most compliance coming from the head of the swimmer and the grip. This means that these components, and not the beam that generates the angular displacement of the tails, will deform most in response to contraction of the muscle. This compliance hinders the performance of the swimmer. The rate of angular displacement of the tails with respect to the displacement of the grips is only 0.072°/μm (Fig. 2E). For a muscle expected to pull the grips by 80 μm, which is our baseline expectation, this corresponds with only 5.8°.

The calibrated angular and translational displacements of the tails with respect to x_3 and x_4 are provided (Fig. 2E). These position values can be more readily quantified through microscope images than either the angular displacement of the tail or the movement of position x_2.

A muscle mounted on the scaffold will have its contraction resisted by half the stiffness measured at a single grip. Sacrificial supports help keep the grips stationary, while the muscle is mounted, and these supports increase the overall stiffness of the scaffold temporarily (Fig. 2D). Before these are removed, the stiffness felt by the muscle is 0.9 μN/μm, behaving linearly up to around 400 μN. If the sacrificial supports are removed immediately, then the overall stiffness drops to 0.8 μN/μm and fall gradually, as the muscle develops tonic tension and shortens. By the time the muscle length has shortened 800 μm, the stiffness has dropped by more than half. As a result, if the sacrificial supports are removed after several days, then the drop in stiffness is larger. Using this property of the scaffold, we can explore the effect of sudden drops in mechanical stiffness on the development of tonic tension in the muscles.

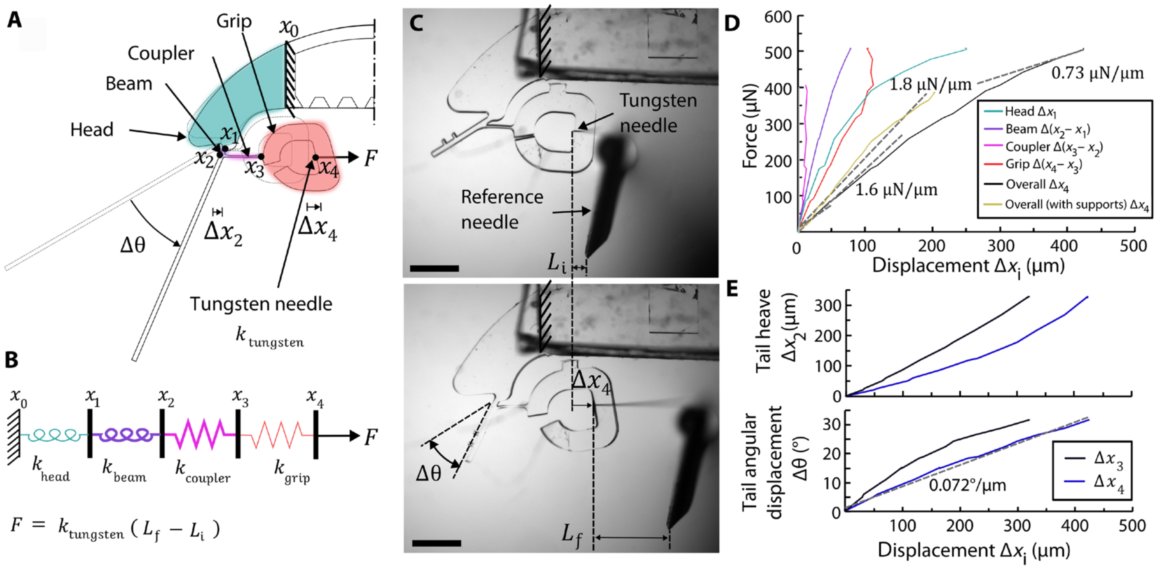

Fig. 2. Calibration of the PDMS swimmer scaffold. (**A**) Schematic of the swimmer scaffold decomposing the overall system into four compliant components. (**B**) An equivalent spring diagram of the compliant components of the scaffold. The head and the beam contribute to the angular displacement of the tail. (**C**) Diagram of the setup for calibrating the PDMS scaffold with respect to the stiffness of a tungsten needle (0.43 μN/μm). A hypodermic needle that moves with the tungsten needle acts as a reference. (**D**) Force-displacement relationships for the components of the scaffold. (**E**) Calibration curves for approximating the tail angular and translational displacement from position values that can be more accurately quantified from images.

Timeline for biological component assembly

The timeline for the fabrication and assembly of the biological components of the swimmer is tracked with respect to when the muscle rings are seeded, on day in vitro (DIV) 0. The biofabrication process involves three key steps (Fig. 3A). These are the seeding of the muscle rings (Fig. 3B), the mounting of the muscle rings onto the swimmer scaffold (Fig. 3C), and the introduction of motor neurons into the head of the swimmer (Fig. 3D). Swimmers are typically ready for swimming on DIV 10 (Fig. 3E).

The biofabrication process involves a few tunable parameters including the time point when the sacrificial supports are cut after the mounting of the muscle ring and the time point when the motor neurons are added to the head of the swimmer. In the following sections, we investigate the effects of cutting the sacrificial supports on the development of tonic tension in the muscle.

The muscle ring seeding process (Fig. 3B) and the muscle ring mounting process (Fig. 3C) are shown in movie S1. Briefly, C2C12 myoblasts are mixed with type I rat tail collagen and Matrigel. The mixture is dispensed into ring-shaped molds with 3-mm inner diameter, which have been coated with a surfactant to reduce cellular adhesion. The samples are inundated with growth medium and the mixture of myoblasts and ECM compact around the centers of the molds (Fig. 3B). After 2 days, a pair of tweezers is used to maneuver the rings into the grips of the swimmer. The maneuvers with tweezers are rendered in Fig. 3C. After mounting, the muscle rings are switched to differentiation medium (see Materials and Methods).

By DIV 8, small, localized spontaneous twitching is usually visible along the surface of the tissue. At this time, motor neurons may be added to the swimmer. This requires (i) injecting the motor neurons along with ECM into the holder on the head of the swimmer and (ii) forming a bridge of ECM between the muscle and the neurons. To do this, the swimmers are removed from their dishes and placed on a hydrophobic surface, in this case, wax paper. The hydrophobicity of the substrate causes medium to form a protective bubble around

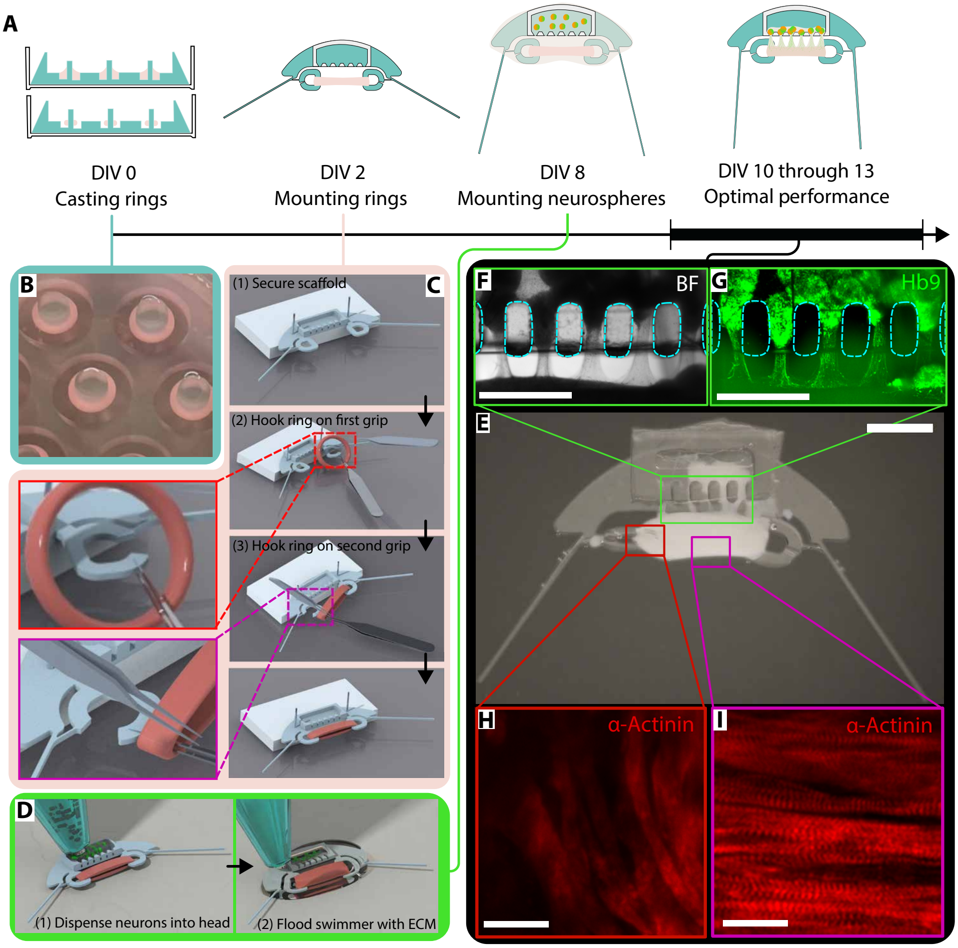

Fig. 3. Timeline for the biofabrication of the swimmer. (**A**) Overall timeline for the biological components. Some preparation steps occur beforehand, including the expansion of a culture of C2C12 myoblasts and the differentiation of mESCs into motor neuron spheroids (see Materials and Methods). (**B**) Ring molds used for casting the muscle tissue rings. (**C**) Renderings of the steps involved in mounting the muscle rings on the scaffold. Callouts show tweezer placement necessary to put the muscle into the grips without causing damage. (**D**) Renderings of the steps involved in mounting the motor neuron spheroids in the head of the swimmer. A hydrophobic paraffin wax substrate causes the ECM to form a bubble around the swimmer. (**E**) Photograph of the swimmer (scale bar, 2 mm) with callouts showing (**F** and **G**) the live bright field (BF) and confocal imaging of the growth of neurites toward the muscle (scale bars, 1 mm) and (**H** and **I**) confocal images of sarcomeric α-actinin assembled into sarcomeres localized in the middle of the muscle tissue taken after fixing (scale bars, 25 μm). The neurite GFP signal indicates expression of the Hb9 motor neuron–specific promoter, although other types of neurons are present in the neurospheres due to incomplete differentiation. The photograph of the swimmer was postprocessed by darkening the background around the edge of the PDMS scaffold to help the clear rubber body stand out.

the swimmer. Next, this medium bubble is aspirated, and the motor neuron spheroids mixed with type I collagen and Matrigel are injected into the holder. Ten microliters of ECM is placed in a new bubble around the entire swimmer (Fig. 3D). This bubble continues to protect the muscle and neurons while the ECM gels. Once the ECM has gelled, the low affinity of the hydrophobic wax paper for the ECM allows us to lift the swimmer along with the ECM off the paper and into a dish. The swimmer is then inundated in coculture medium. During inundation, the surface tension of the medium will tend to disrupt the ECM gel, causing any loose fragments to fall off. When the gap between the muscle and the neuron holder is small enough, ECM gets trapped in this cleft and acts to connect the muscle to the neurons.

At this point, the biofabrication process is finished, and the rest of the changes to the swimmer are the result of self-assembly (Fig. 3E). Over the 2 days following the addition of motor neurons, any loose ECM is pulled into the muscle by the C2C12 cells, leaving only the bridges of ECM that are pulled taut between the motor neurons and the muscle (Fig. 3F). By DIV 10, motor neurites tagged at the Hb9 promoter with green fluorescent protein (GFP) for live imaging are seen to grow along these bridges toward the muscle (Fig. 3G). When the swimmers are fixed after DIV 13 and stained for sarcomeric α-actinin, we find cross-striated myofibers in the middle of the tissues (Fig. 3I), with less organized structures around the grips (Fig. 3H). This evidence of sarcomeres suggests that the muscle is developing but not necessarily uniformly across the tissue.

Neurospheres in the head of the swimmer are liable to shift and compact, which can lead to asymmetric distribution in the head of the swimmer (Fig. 3E). Other examples of neurosphere distributions are provided (fig. S1).

Muscle development is robust against stiffness perturbation, stiffness history, and small stiffness variation

The compliant mechanism necessitates the addition of sacrificial supports connecting the muscle grips to the head of the swimmer. Each of the sacrificial supports acts as a spring in parallel to the rest of the compliant mechanism (Fig. 4A). On DIV 2, muscle rings are mounted on the swimmer scaffolds with the sacrificial support intact. After mounting, the mechanical stiffness felt by the muscle is 0.9 μN/μm. Removing these supports changes the stiffness felt by the muscle. The sacrificial supports can be removed immediately after mounting or after several days. To choose the best time point to remove the supports, we investigated how the muscles would respond to the sudden disruptions to their mechanical anchorage in the short term and how they would respond to varying mechanical anchorage in the long term. To do this, we removed the sacrificial supports on different days in the timeline of muscle maturation (Fig. 4A). We take the tonic tension in a developing muscle tissue as an indicator of maturation because it has been found to precede the formation of immature myofibrils and spontaneous twitching (*42*).

We can track the tonic tension in the muscle by measuring the distance between the points marked x_3 on both sides of the muscle or by the change in the resting angle of the tails $\Delta\theta$ (Fig. 4B). Both the translational and angular force-displacement curves for the compliant mechanism exhibit nonlinear softening (Fig. 4C), and this is because the head of the swimmer will tend to bend out of plane around a tension of 400 μN.

We prepared three groups of swimmers for which the sacrificial supports would be cut on DIV 3, 6, or 9, respectively. These days were chosen because we expected the muscle to start twitching and responding to electrical stimulation around DIV 8, and so these 3 days correspond with early, mid, and late differentiation. Cutting the supports on DIV 3 gives the muscle tissue time to acclimate to the new culture condition after being transferred onto the swimmer scaffold on DIV 2.

In this experiment, muscle rings were mounted on 11 swimmer scaffolds on DIV 2 and inundated in differentiation medium. Every day, their length and approximate tonic tension were recorded. The 11 swimmers were separated into three groups, with the sacrificial supports being cut on different days for each group. After the sacrificial supports are cut on DIV 6 and 9, there is an immediate shortening of the muscle as it loses tension, followed by a rapid shortening over the next day (Fig. 4D). The tonic force data shows two key results (Fig. 4E). First, following the removal of the sacrificial supports, the muscles rapidly shorten and develop back to the same tonic force level within 12 to 15 hours. Fitting the change in tonic tension during these periods to an exponential trend, we find time constants for tension restoration between 4 and 6 hours. This suggests that the muscles have some mechanism that drives their tonic tension to a homeostatic value in the event of a mechanical perturbation. We also see that this homeostatic value is varying from day to day, leveling off around DIV 11, at an average tonic tension of 536 ± 112 μN ($n = 11$, means ± SD). The second result is that the homeostatic tension between the populations is insignificantly different every day, except DIV 4. This is noteworthy because the muscles in the different sample groups are working against a different mechanical stiffness on any given day. The difference in the mechanical stiffnesses felt by different muscles is within a factor of 2, so if the homeostatic tonic tension in the muscles is mechanosensitive, then the variation in stiffness may be insufficient to induce a noticeable variation. Although more investigation is required, we currently hypothesize that for a range of low stiffness anchors within the neighborhood of 1 μN/μm, the tonic tension in the muscle tissue is invariant to changes in stiffness.

Motor neurons increase spontaneous and evoked muscle contractility

Muscle contraction is driven by actomyosin machinery inside of the individual muscle fibers. In their immature state, C2C12 muscle tissues have been shown to express Connexin 43 gap junctions (*56*), and so many connected, immature muscle fibers will tend to contract as a single unit. Because the refractory period for the depolarization of muscle is only 2 to 3 ms (*57*), the contraction cycles of a muscle can overlap. At low-frequency stimulation, a muscle can relax between depolarization events, leading to single isolated twitches. At higher frequencies, the muscle cannot fully relax between depolarizations, leading to an accumulated shortening referred to as tetanus. The muscle is said to exhibit unfused tetanus if the individual contractions are still distinguishable and fused tetanus if the individual contractions become indistinct (Fig. 5A) (*58*).

We are interested in the percent change in the length of our muscle rings due to electrical stimulation because this limits the amount of actuation the muscle can supply to the tails of the swimmer (Fig. 5B). Muscle rings are electrically stimulated using a pair of graphite electrodes spaced 2 cm apart on either side of the swimmer. With increasing stimulation frequency, we see the muscle transition from single twitches to unfused tetanus (Fig. 5C). Because of summation, the contractility of the muscle is higher when subject to higher frequency stimulation, but this accumulated tetanic contraction does not have time to fully relax in the 10-s period between different

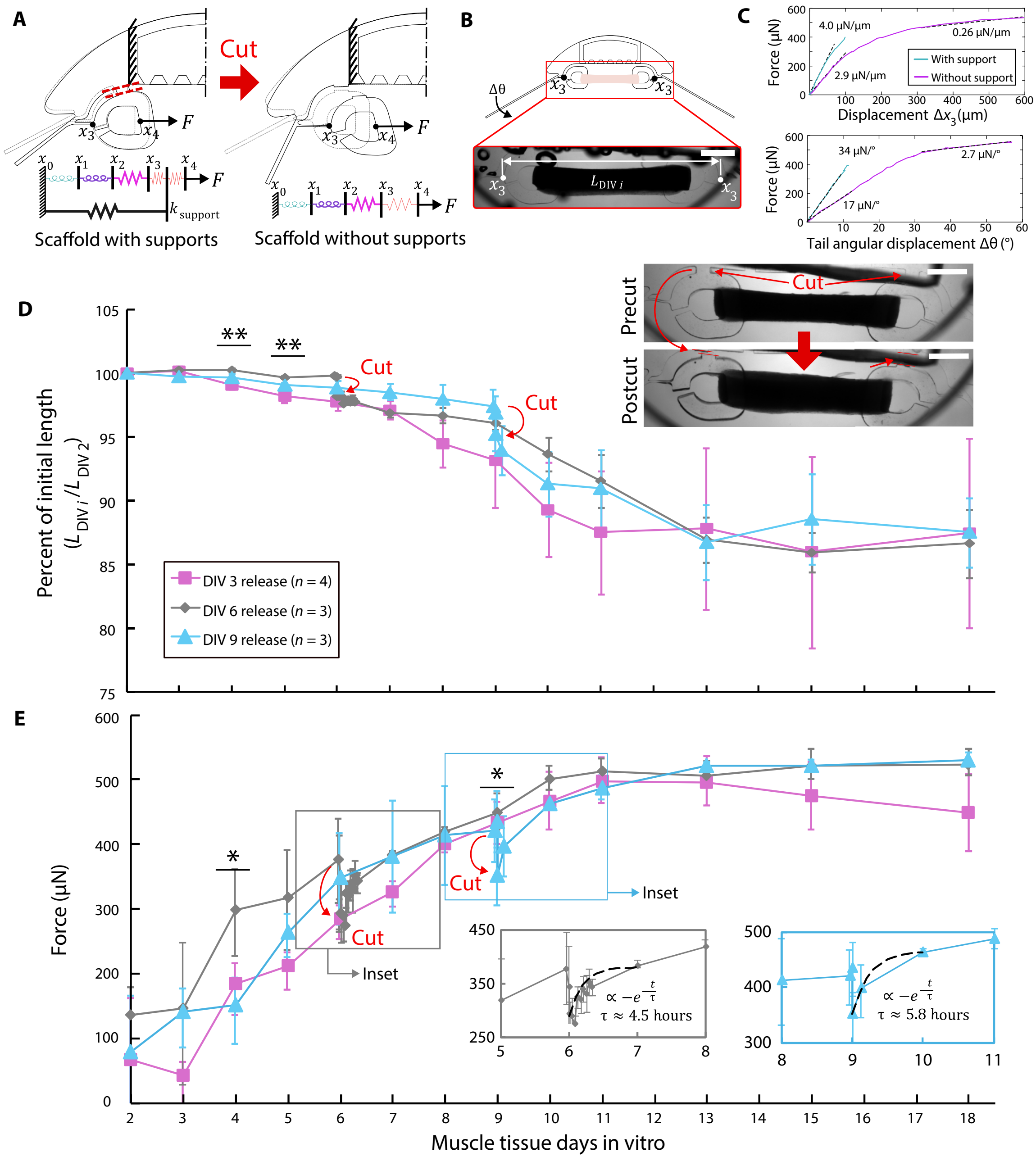

Fig. 4. Muscle shortening and tonic force during development. (**A**) Schematic showing the change in scaffold geometry following removal of the sacrificial supports. (**B**) Diagram defining how the contraction of the muscle is quantified from bright field images. (**C**) Force-displacement curves for calculating the tonic tension in the muscle before and after removal of the sacrificial supports. (**D** and **E**) Tracking the variation in the muscle length and tonic force in three groups of swimmers. The groups specify whether the sacrificial supports are removed during early, mid, or late differentiation. Statistics indicate the results of one-way analysis of variance (ANOVA) statistical tests comparing the percent of initial lengths of the muscle of the three groups (**$P < 0.01$; *$P < 0.05$). For DIV 6 and 9, statistics reflect length measurements taken 1 hour after the removal of the sacrificial supports. By DIV 9, after cutting the sacrificial supports on the last group of samples, large variation among the muscle lengths contributes to the groups being indistinct from one another ($P > 0.05$ by one-way ANOVA). Insets show the change in force following the removal of the sacrificial supports on DIV 6 and 9. Exponential curve fits give approximate time constants of 4.5 and 5.8 hours for recovery of the force during the 24 hours after release.

stimulation frequencies. At 1-Hz stimulation, muscle contractility increased with the electric field strength up to 8 V/cm and then plateaued (Fig. 5D). High voltages sometimes excite spontaneous twitching, and this hindered our ability to control the swimmer. Because of this, we performed all our subsequent experiments with 3 V/cm.

To investigate how the introduction of motor neurons would affect muscle contractility, we prepared two batches of swimmers, one with only muscle and one with muscle and motor neurons in coculture. We chose to compare their contractility around DIV 10 because, at this time point, all of the muscles responded to electrical stimulation. We observe that starting around DIV 10, the muscles in coculture

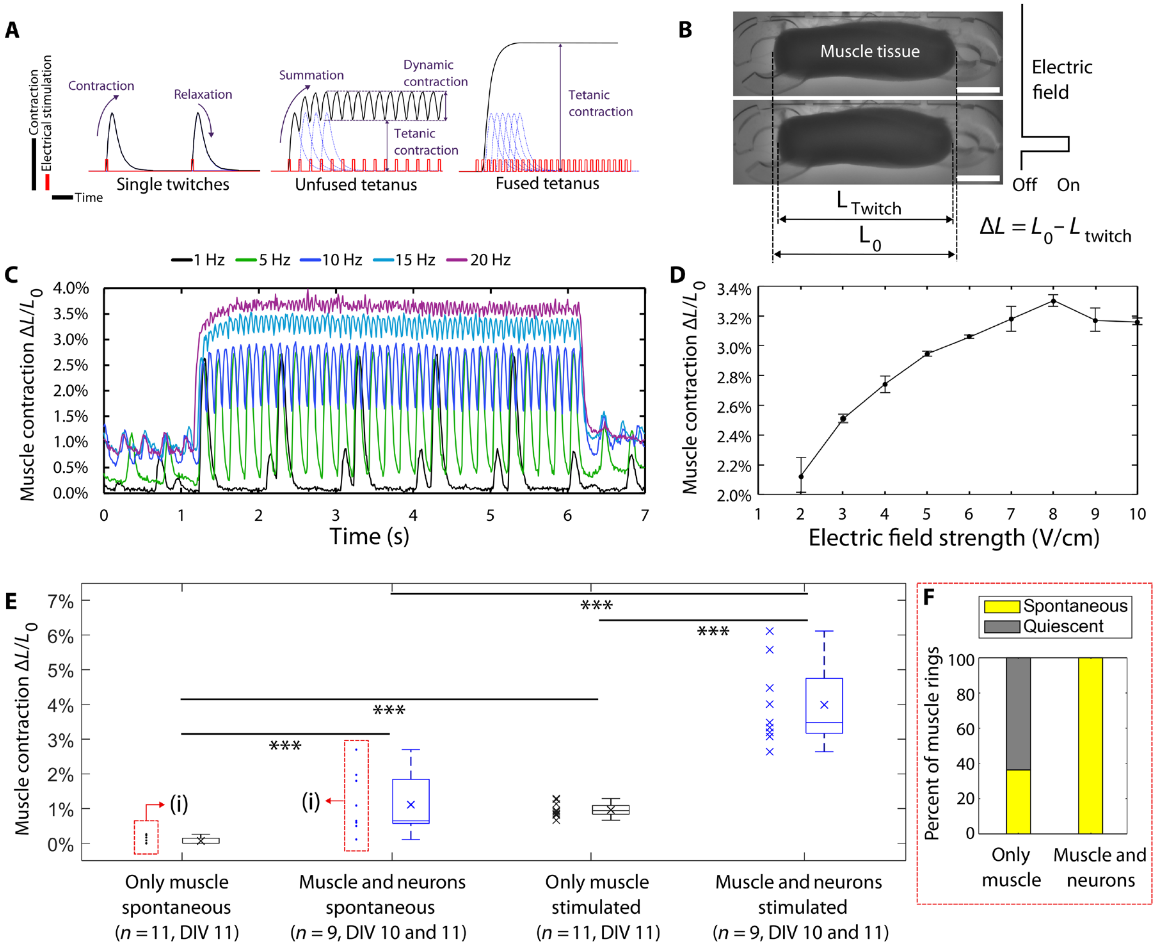

Fig. 5. Characterization of the spontaneous and evoked contractility of the muscle tissues. (**A**) Nomenclature used to describe muscle contraction at different stimulation frequencies. (**B**) Schematic defining how muscle contractility is measured with respect to the resting length of the muscle. (**C**) Variation in the muscle contractility and dynamics with increasing frequency for a typical swimmer. Low-amplitude spontaneous twitches (~1%) can be seen interspersed with the evoked spikes. Measurements are with respect to the length of the muscle before any stimulation occurred, so the offset at the start of higher frequencies is persistent tetanic contraction. (**D**) Variation in peak contractility with increasing electrical field strength for a typical swimmer ($n = 4$, means ± SD). (**E**) Comparison of the spontaneous and evoked contractility (stimulation, 3 V/cm) of swimmers with and without the inclusion of motor neurons. Statistics refer to t tests assuming independent samples (***$P < 0.001$). Individual measurements are shown beside their corresponding box plots. "x" annotations indicate the mean of each group. (**F**) The percentage of muscles in each group that exhibited any spontaneous twitching at the time of the experiment. The highly significant comparison between the spontaneous twitching activities of the two groups includes quiescent, muscle-only swimmers. If instead these are disregarded, then the spontaneous contractility of the groups is not significantly different ($P > 0.05$).

with motor neurons exhibit strong, frequent spontaneous twitching, visible to the naked eye (movie S2). The muscles by themselves sometimes exhibit spontaneous twitching. As a note, the serum concentration is the same for all swimmers after DIV 2 (2% horse serum), but the basal medium varies between muscle-only and cocultured swimmers with Dulbecco's modified Eagle's medium (DMEM) in the aneural samples and a 50:50 mixture of advanced DMEM/F-12 and Neurobasal Plus medium in the cocultured samples. On DIV 10 and 11, we take recordings of the swimmers subject to 1-Hz electrical stimulation at 3 V/cm (Fig. 5E). If the muscles are twitching spontaneously at the start of the recording before electrical stimulation is applied, then we note the amplitude. It was observed that all of the cocultured swimmers were twitching spontaneously before electrical stimulation as compared to only 36% of the muscle-only swimmers (Fig. 5F). In both groups, spontaneous twitching amplitude is highly variable, and if we only consider the swimmers that were twitching spontaneously, then there was no significant difference in their contractility. If we consider all the swimmers and say that quiescent muscles have zero spontaneous contractility, then the difference between the groups is highly significant ($P < 0.001$). We interpret this to mean that cocultured swimmers are significantly more likely to be twitching spontaneously on DIV 10 but that the amplitude of spontaneous twitching is not significantly more than in muscle-only swimmers. All swimmers in both groups were observed to respond to electrical stimulation. On average, the cocultured swimmers exhibited 4.2 times higher contractility than the muscle-only swimmers.

This improvement in contractility in the cocultured swimmers was observed 2 days after the introduction of the motor neurons. On this day, neurites can be observed in the ECM bridges between the swimmer's head and the muscle and in contact with the muscle ring (Fig. 3G). Previous studies have not observed functional NMJ formation in vitro before 5 days (*12*, *31*, *34*), so at this early time point, we hypothesize that there is some chemical signaling via soluble factors between the motor neurons and the muscle, which is causing the muscle to twitch.

Concerning the long-term stability of the swimmers, we found that beyond 2 weeks, the performance of the swimmers declines until they no longer respond to electrical stimulation. Previous studies have identified similar decline in engineered skeletal muscle because of proteolytic degradation (*59*). They have also shown that culturing muscle with E-64, a broad-spectrum cathepsin inhibitor, can extend the lifespan of C2C12 tissues to more than 200 days (*60*). In our case, as early as DIV 11, we begin to observe lumps on the side of the muscle tissue, which sometimes respond to electrical stimulation by twitching (fig. S2A). We suspect that these are recoiled myotubes, which lost their anchorage and buckled on themselves because of their tonic tension. In addition, by DIV 11, we see that proliferative myoblasts leave the tissue, which, over several weeks, proceeds to cover the swimmer scaffold. This may suggest that the loss of mechanical anchorage is less an issue for the undifferentiated myoblasts. We suspect that over time, the muscles become overrun with myoblasts. Long term, the muscle can also fail. One way they can do this is by bending the grips open and sliding into the 90° corner made by the PDMS. The muscle will then slowly begin to thin at this point before eventually tearing off (fig. S2B). This slow tearing may be the same necking process observed for C2C12 muscle tissues on other platforms (*61*). Sliding into the corner of the grip lowers the effective cross-sectional area of the tissue, which might lead to an instability. Failure may also happen if the muscle tissue sustains damage during the mounting process, such as an indent that lowers the effective cross-sectional area at a distinct point. In one interesting case, the muscle failed at one of these necking points, and the two free ends became incorporated into the other side of the muscle ring, changing the muscle topology (fig. S2C).

Swimming experiments

Low-*Re* theory for flagellate swimmers predicts thrust generation that varies with actuation amplitude and frequency. We want to see how our swimmers' performance compares with our low-*Re* simulations. In living creatures, motor neurons can recruit different numbers of motor units and stimulate them at high frequency to achieve fine control of force and position. With electrical stimulation, we are more limited in how we can drive our muscle rings. After suspending our swimmers in a fluid density gradient to keep them away from surfaces, we stimulate them with electrical pulses at varying frequencies. From recordings taken on an inverted microscope (Olympus IX81), we can track the position of the swimmer over time and the contraction of the muscle (Fig. 6A). We can feed the muscle contractions back into our low-*Re* model for a direct comparison between theory and experiment. In the following section, we describe our experimental setup and visualize how the swimming behavior varies with stimulation frequency. Then, we use particle streak imaging to investigate why our experimentally measured swimming velocities vary strongly with tail angular displacement while deviating from low-*Re* predictions. This leads us to consider the role of the contraction velocity of skeletal muscle and how it might allow for faster biohybrid swimmers.

Analyzing swimming velocities

Swimmers exhibiting strong contractility (>2%) to stimulation at 3 V/cm are placed in a dish containing a mixture of coculture medium and Percoll (P1644, Sigma-Aldrich). The density of PDMS (1.06 g/ml) is slightly higher than cell culture medium, and the density of Percoll is slightly higher than PDMS, so the swimmer will tend to float at the Percoll and culture medium interface due to buoyancy (fig. S3A). Of the 12 swimmers prepared following the timeline in Fig. 3, 11 exhibit a response to electrical stimulation, of which 6 exhibit forward swimming. Of the other five, two only exhibited

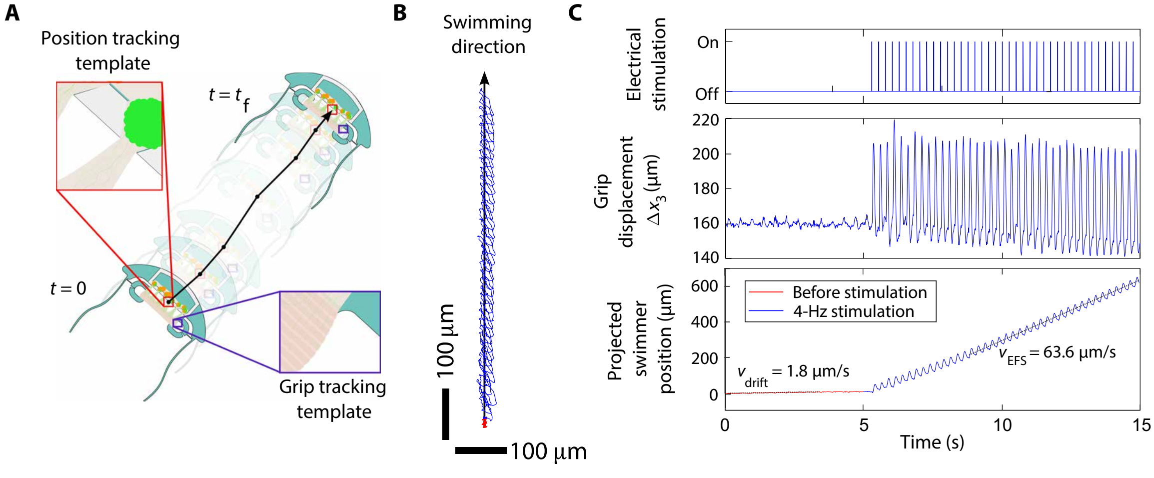

Fig. 6. Swimming position tracking and analysis. (**A**) Diagram of the template tracking method employed to quantify the swimmer's position and muscle contraction waveforms. (**B**) 2D projection of the path of a point on the head of the swimmer before (red) and during (blue) 4-Hz electrical stimulation. (**C**) The corresponding stimulation, grip displacement, and position of the swimmer during the 4-Hz electrical stimulation. The position is taken by projecting the swimmer's path onto the direction of travel. Before stimulation, the swimmer drifts with a small velocity. This is attributed to currents in the dish caused by air movement at the free surface and vibrations. Because features normal to the plane of the swimmer scaffold, such as the side of the neuron holder, are visible in microscope recordings, we infer the swimmer is floating with a nonzero angle of attack. When the muscle contracts, the projected length of these features is observed to change as the swimmer pitches forward and backward (fig. S3B). An estimate from these motions gives that the swimmer sits at 16° from the plane of the microscope and pitches 1° to 2° every time the muscle twitches (fig. S3C).

weak contractility, one swam in circles due to a grip getting stuck, and two moved erratically and only at speeds comparable to the drift in the dish (~1 μm/s). Swimmers are subject to electrical stimulation and recorded. From each recording, their position over time is extracted using an ImageJ template matching plugin (Fig. 6A) (*62*). Points tracked on the body of the swimmer tend to oscillate with an overall straight trajectory (Fig. 6B). The projection of the swimmer trajectory in the direction of travel is used to define the velocity of the swimmer before and during electrical stimulation (Fig. 6C). Contraction of the muscle is calculated by tracking a point on the grip with respect to the head of the swimmer and then adding the displacement of the grip due to the tonic contraction of the muscle. At rest, the swimmers are observed to drift at speeds around 1 to 2 μm/s. This is attributed to currents in the medium caused by air movement at the free surface above the cell culture medium. In the example (Fig. 6C), the swimmer moves with a time-averaged velocity of 63.6 μm/s during 4-Hz stimulation, which corresponds to a *Re* of 0.33 (movie S3). During each muscle twitch, the tails experience a peak angular displacement of 4.8° ± 0.25° (n = 39, means ± SD). This is derived from the grip displacement (Fig. 6C) using the calibrations for tail angular displacement in terms of x_3 (Fig. 2E). The resting tail angle is 38° from the direction of swimming.

Persistent motion of the swimmer over multiple stimulation frequencies

To see how stimulation frequency affects swimming, we ran each of the swimmers through a sweep of 11 frequencies between 0.5 and 20 Hz over the course of 2 min. Stimulation was applied at each frequency for 5 s with a 5-s rest between frequencies. From recordings of each of these tests, the position of the swimmer and the contraction of the muscle were extracted, allowing us to assess the swimming speed of the swimmer with respect to the actuation from the muscle. An example of these data for a single test is given in Fig. 7 (A to D) (movie S4). From the muscle-driven grip displacement (Fig. 7C), we can approximate the grip velocity. In addition, from the swimmer position over time (Fig. 7A), we can approximate the swimming direction, project the position of the swimmer over time along the swimming direction (Fig. 7D), and compute a time-averaged velocity for the swimmer at each frequency. The computed time-averaged velocities for this swimmer at each frequency are presented alongside the measurements for the other five swimmers (Fig. 7E). The highest time-averaged swimming velocity among all swimmers was 86.8 μm/s (0.58 body lengths/min). At frequencies of ≤5 Hz, the swimmer reaches a steady time-averaged velocity within a few stimulation cycles, and so the velocity is well defined. When stimulation ends, the swimmer is observed to decelerate (case 1). At frequencies of ≥8 Hz, the onset and relaxation of unfused tetanus in the muscle causes large transients in the swimmer's motion. Toward the end of each 5-s stimulation period, the swimmer appears to reach a steady time-averaged velocity, here denoted v_{steady} (Fig. 7D). The duration of the transient in the swimmer's velocity between the time of tetanus onset and reaching this steady state is another instance of where the swimmer seems to decelerate (case 2). When stimulation at these frequencies ends, the tetanic contraction relaxes causing the swimmer to lurch backward with a high velocity, after which it decelerates (case 3).

We draw attention to these three cases of deceleration because they are evidence of inertia contributing to the swimmer's displacement. In the regime of vanishing *Re*, instantaneity holds that a deforming body in a fluid stops moving the instant it stops deforming (*21*, *22*). With increasing *Re*, inertia contributes more to the swimming mechanism. The body coasts on momentum for a much longer distance before it is stopped by viscous drag. With increasing *Re*, we begin to describe the motion of the body as ballistic.

We investigated the source of the swimmer's deceleration with a model of ballistic motion, which only accounts for the drag force. We suppose that the swimmer has mass m and experiences drag proportional to its velocity with a constant drag coefficient γ. In addition, we suppose that the swimmer has some initial velocity v_0 and position x_0 at time t_0. Let $x(t)$ be the position of the swimmer over time in the laboratory reference frame where the fluid is drifting with some small velocity v_{drift}. From the force balance, we have it that $m\ddot{x} = -\gamma\left(\dot{x} - v_{\text{drift}}\right)$. Solving the initial value problem gives $x(t) = v_0 \frac{m}{\gamma} e^{-\frac{t-t_0}{m/\gamma}} + v_{\text{drift}}\left(t - t_0\right) + x_0$. The characteristic time constant τ for the deceleration is mass divided by the linear drag coefficient, $\tau = m/\gamma$. We fit experimentally measured $x(t)$ of the swimmer to the above equation for the following three cases: 1 s after the end of 0.5- to 5-Hz stimulation (Fig. 7F), during 8- to 20-Hz stimulation when muscle reaches tetanus state with subsequent low-amplitude contractions (Fig. 7G), and 1 s after 8- to 20-Hz stimulation is stopped (Fig. 7H). The relevant corresponding data are called out in Fig. 7D. The delay of 1 s is introduced to remove any transient dynamics, which occur immediately after starting or stopping stimulation. All the data in Fig. 7D come from a single swimmer with a wet mass of ~27 mg. On the basis of the speed of the swimmer at the start of the experiment, the drift velocity v_{drift} is ~1.76 μm/s. Each curve fit for each case yields a slightly different value for the time constant τ, with an average value of 2.8 s. Using τ = 2.8 s, we repeat the fitting to calculate values for v_0 and x_0. Using these values for v_0 and x_0, each of the curves can be nondimensionalized to isolate the first-order dynamics.

The velocities seen for this example swimmer range from 10 to 80 μm/s, which corresponds with $Re \sim \mathrm{O}(10^{-1})$. At intermediate values ($Re \sim 1$), we would expect both the inertial and viscous forces to contribute to the thrust generating mechanism of the swimmer. Whereas viscous forces contribute to propulsion through drag asymmetry of the tails, inertial forces would contribute by imparting momentum to the surrounding fluid. This regime of *Re* is not considered for flagellate swimmers (*12*, *38*).

For a wet mass of 27 mg, the average time constant of 2.8 s corresponds to a linear drag coefficient of 9.6 mg/s. This is lower than the predicted drag for the two tails, $\gamma_{\text{tails}} = 21.6$ mg/s. It is also lower than our full prediction of the drag of the swimmer that includes the head drag, γ = 42.6 mg/s (for a projected forward cross-sectional area of 3 mm^2). In the following section, a low-*Re* model of the swimmer dynamics is given the tail boundary conditions from our experiments. The model is used to predict the velocities we would expect for swimming at low *Re*. This calculation assumes that the swimmer comes to rest immediately once the propulsion force F_{prop} from the tails is removed, such that the velocity $v(t) = F_{\text{prop}}/\gamma$.

Comparison between experimental swimming and low-Re simulations

To assess the agreement of our experiments with low-*Re* elastohydrodynamic model predictions (*39*), we simulated swimmer velocities for drag coefficients γ = 9.6 and 42.6 mg/s, using experimental muscle contraction waveforms for stimulation frequencies between 0.5 and 5 Hz and for angular displacement amplitudes between 0° and 8° (see Materials and Methods). These simulations produce regions of predicted velocities that depend on tail angular displacement

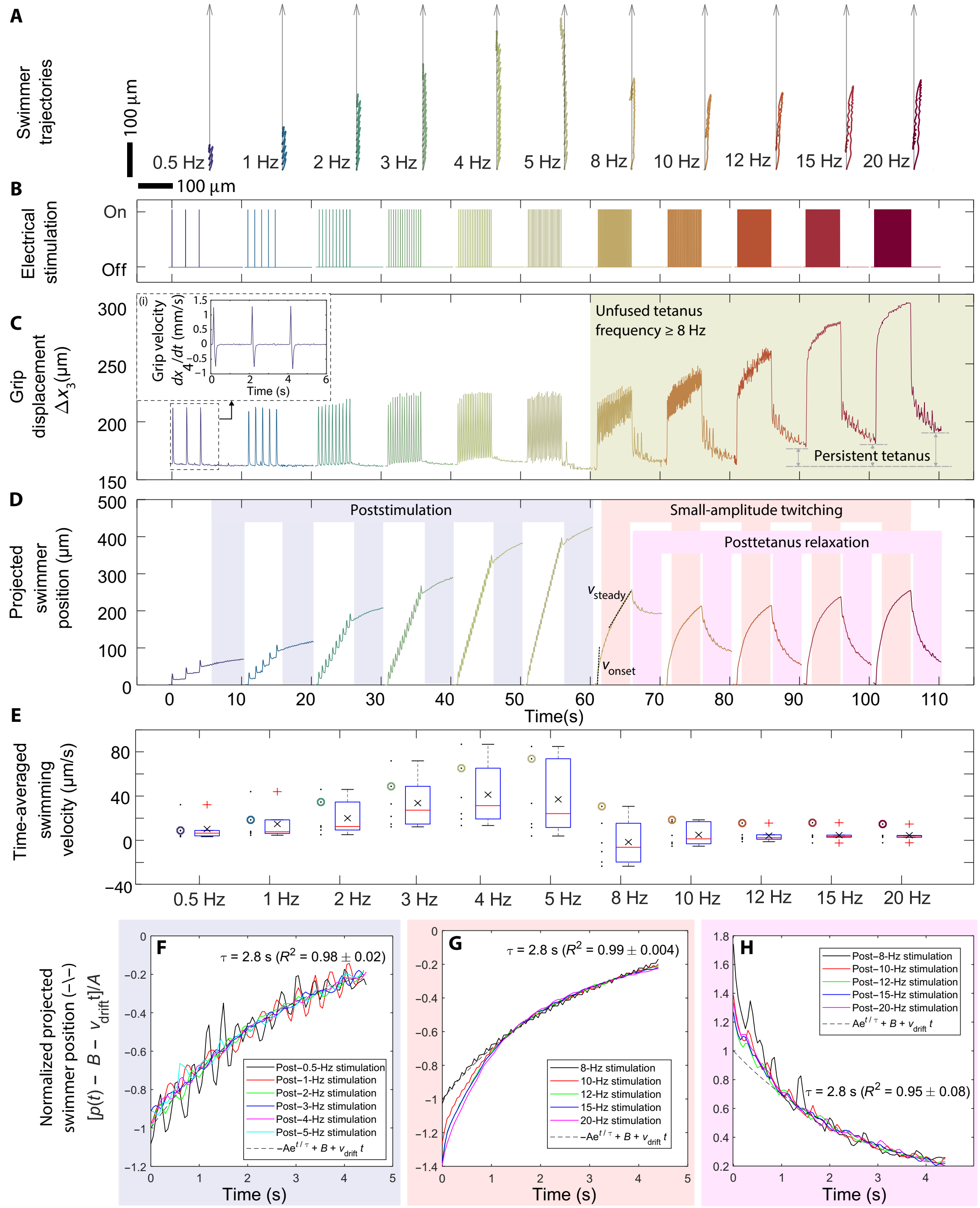

Fig. 7. Swimming waveforms for a high performing swimmer. (**A**) *x-y* coordinate plots for the swimming trajectory at multiple frequencies. (**B**) Electrical stimulation waveforms (3 V/cm, 10-ms pulse width). (**C**) Muscle contraction measured from motion of x_3, the junction between the grip and the coupler. Inset: Grip velocity measured from the attachment of the muscle x_4. (**D**) Swimmer displacement projected along the swimming trajectory. At frequencies of ≥8 Hz, the onset and relaxation of tetanus give the position waveform a distinct sawtooth shape. (**E**) Aggregated time-averaged swimming velocities for all swimmers at each frequency. Circled data correspond with the example swimmer presented in (A) to (D). (**F** to **H**) Nondimensionalization of the swimmer dynamics with time constant τ = 2.8 s for each of the cases. Background colors refer to time windows in (D).

and the range of frequencies considered (Fig. 8A). Neither drag coefficient yields velocity predictions above 40 μm/s. When we plot all our experimental time-averaged velocities (Fig. 7E) against their corresponding tail angular displacement amplitudes, we see a sharp increase in swimming speed for tail angular displacements above 4° (Fig. 8A). When we look at the comparison of experimental and simulated measurements for the example swimmer, we see again higher time-averaged velocities than those predicted for the experimental tail boundary conditions (Fig. 8B). If there is a transition in the swimming dynamics as the tail angular displacement amplitude increases, then we hypothesize that it would be possible to visualize this transition by visualizing the flow around the tail with tracer particles.

Flow field visualization with particle streak imaging

To visualize the flow field, we affixed a swimmer scaffold to a post in the middle of a polystyrene dish, filled the dish with a mixture of Percoll, saline, and tracer particles, and used a programmable micromanipulator to pull on the grips of the scaffold in place of a muscle. The amount of Percoll was tuned so that the interface between it and the saline would lie at the level of the swimmer's tails. This setup replicates the conditions of the biohybrid swimmer experiments, with saline standing in for cell culture medium. Polystyrene beads (15.45 μm in diameter) with a density higher than Percoll but lower than saline (1.05 g/cm^3) are added as tracer particles to the dish. Because of the density gradient, the beads tend to settle on the same plane as the Percoll-saline interface and the tail. Tracer particles follow the flow with high accuracy if their Stokes number (Stk) is small, i.e., $Stk \ll 1$ (*63*). The Stokes number is a dimensionless parameter that represents the ratio of the characteristic time it takes the particles to respond to a flow to the characteristic time scale of the flow. For these beads, $Stk \sim O(10^{-3})$, and so we conclude that they are suitable for this experiment (see Materials and Methods). Using the programmable micromanipulator, we control the velocity of the grip and can reproduce grip velocities up to and above the peak grip velocities observed in the swimmer experiments (Fig. 9B), which range between 600 and 1800 μm/s (Fig. 9C).

For every pair of grip velocity and tail angular displacement considered, we record the movement of the tracer particles over the course of 5 cycles of periodic tail motion. Each cycle consists of the grip moving according to a symmetric, trapezoidal wave with fixed speed and a defined maximum displacement. We include a 0.1-s dwell time at the peak of the waveform and a 1.1-s dwell time between each cycle to allow the flow time to settle (see example cycle waveforms in Fig. 9B). When we invert the pixel values in the recording and take a maximum intensity projection through the image stack, we end up with streak images that show the paths of the tracer particles. We tag the initial and final position of each particle with red and blue dots. The complete set of these images are available in movie S5.

We see from these images a change in the behavior of the particles with increasing tail angular displacement above a threshold grip velocity which lies between 460 and 900 μm/s. Below this threshold at a grip velocity of 460 μm/s, the tracer particles follow tight elliptical paths with minimal net displacement, even for 20° angular displacement (Fig. 9D). The elliptical paths overlap, making them difficult to distinguish. Individual particles can also be tracked for high-resolution determination of the particle paths. Above the threshold, at a grip velocity of 2300 μm/s, the tracer particles near the tail follow long streaking paths that oscillate back and forth with the tail. We can see two vortices form in the flow field on either side of the tail. We attempt to quantify this change in the flow field with increasing grip velocity by considering the time-averaged velocity of beads in the vicinity of the tail, along the direction of the tail (Fig. 9E). To calculate this, we project a vector pointing from the initial to the final position of a given bead along the direction of the tail and divide its length by the total time it took for the bead to travel that distance. Because of the dwell time, this calculation overestimates the velocity of slow beads and underestimates the

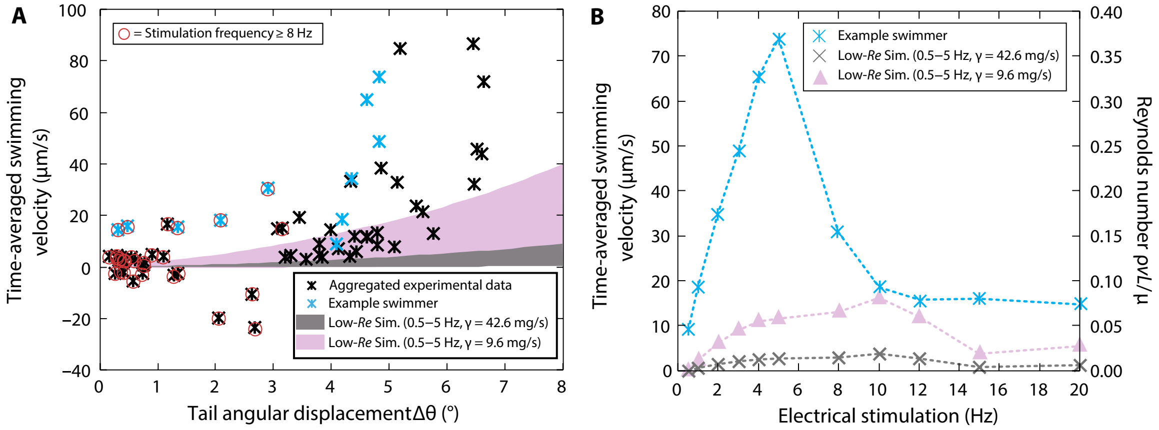

Fig. 8. Comparison between experimental swimmer velocities and predictions from our low-*Re* model. (**A**) Aggregated swimming velocities and tail angular displacement amplitudes across all samples ($n = 6$) compared against regions corresponding to low-*Re* model predictions generated with the indicated frequencies, tail angle changes, and drag coefficients. Tail angular displacement amplitudes correspond with the dynamic contraction (Fig. 5C) of the input waveform, excluding tetanus contraction. Simulations are run using experimental muscle contractions waveforms as the model inputs. Inputs are scaled to achieve the associated tail angular displacement amplitude. Red circle annotations indicate whether a datum corresponds with a frequency, which induces unfused tetanus in the muscle. (**B**) Comparison of experimental and predicted swimmer velocities at multiple stimulation frequencies for a single swimmer. The predicted swimming velocities are generated using the experimental muscle contraction for this swimmer as inputs to the simulation.

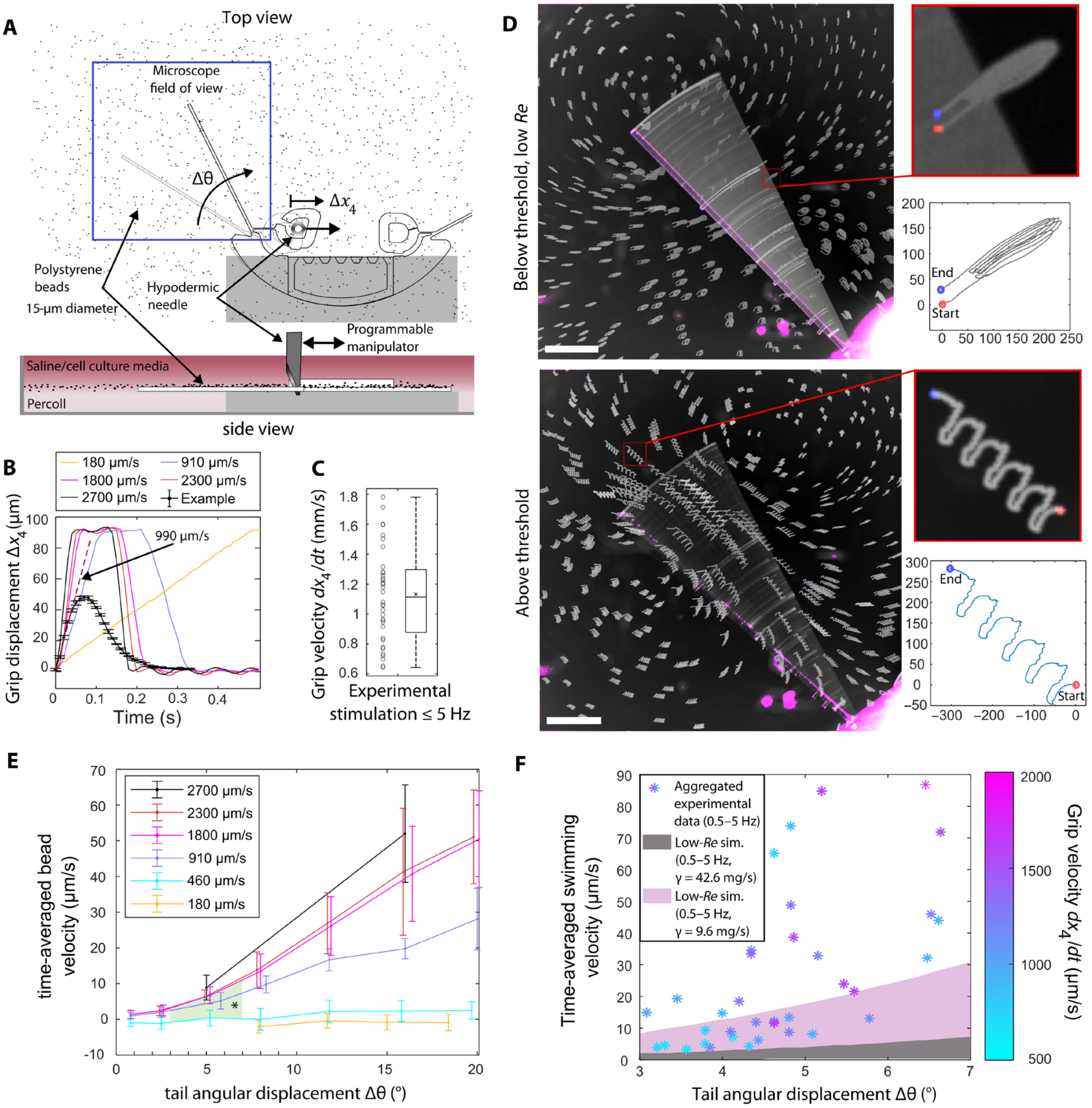

Fig. 9. Particle streak visualization of a flow regime transition due to increasing tail angular displacement amplitude and increasing grip velocity. (**A**) Schematic for reproducing the flow field of the swimmer tail using a micromanipulator. (**B**) Example trapezoidal waveforms by the micromanipulator at different speeds and constant peak displacement, overlaid on a waveform of grip displacement produced by a muscle (taken from Fig. 5C for 1-Hz stimulation, $n = 4$, means ± SD). (**C**) Box plot of the grip velocities observed during swimming of the six for stimulation frequencies between 0.5 and 5 Hz ($n = 36$). Grip velocity values are calculated as the average over all contractions of a muscle at a given frequency while swimming. (**D**) Example particle streak images on either side of the transition corresponding to grip speeds of 180 and 2300 μm/s and maximum angular displacements of 18.5° and 19.8°, respectively. Scale bars, 1 mm. Callouts show example streaks and higher-resolution positional data of the corresponding beads collected using template matching. Units are in micrometers. (**E**) Quantification of the change in the flow dynamics based on the time-averaged velocity of beads in the direction of the tail ($n = 7$, means ± SD). Asterisk (*) indicates region corresponding to our experimental swimming results for stimulation frequencies between 0.5 and 5 Hz. (**F**) Reproduction of the data in Fig. 8A restricted to stimulation frequencies between 0.5 and 5 Hz with corresponding average values of the grip velocity. Grip velocity values are taken as the average over all contractions of a muscle at a given frequency.

velocity of fast beads, providing conservative estimates. This analysis of the time-average velocity of beads along the direction of the tail shows evidence of a threshold grip velocity and a strong dependence of the bead velocity on tail angular displacement for grip velocities above the threshold.

We consider the time-averaged velocities of swimmers subject to stimulation frequencies between 0.5 and 5 Hz (Fig. 7A). Looking at the corresponding values of tail angular displacement amplitude and grip velocity, we see that all data fall within the range of 3° to 7° and 460 to 1800 μm/s, respectively (green "*" region in Fig. 9E). When we plot these data with a heatmap corresponding to the average peak grip velocity, we see lower swimming velocities (<20 μm/s) associated overall with lower grip velocities and higher swimming velocities associated with higher grip velocities (Fig. 9F). The trend of increasing swimming velocities with increasing grip velocity and angular displacement amplitude is consistent with the transition observed in the particle streak imaging data. This suggests that a transition in the swimmer's dynamics accounts for the high swimming speeds we observed and their deviation from low-*Re* predictions.

DISCUSSION

This study takes the design for a theoretically faster, flagellate-type swimmer through the process of biohybrid implementation: solving engineering problems related to scaffold compliance and muscle maturation, examining the effects of scaffold-tissue and muscle-neuron interactions, and lastly investigating the role of inertia in swimming performance. In the following sections, we seek to ground these key findings in their value to the study of biohybrid robotics, myogenesis, and biomimetic small-scale locomotion.

Optimization of the swimmer scaffold

Our swimmer design focuses on converting muscle contraction into large angular displacement of the swimmer tails. The results of the particle streak imaging experiment suggest that this design attained enough angular displacement at a high enough velocity to reach an intermediate-*Re* flow regime (Fig. 9F) and that there is room for further improvement (Fig. 9E). Our calibration of the swimmer scaffold showed that the majority of the muscle contraction was being taken up by the scaffold components we called the grip and the head, and not by the beam, which primarily drives the angular displacement of the tail (Fig. 2D). We would claim that tuning the dimensions of the scaffold to fix this problem is nontrivial. It would require simultaneously balancing the optimal scaffold stiffness for the muscle, around the limited contraction of the muscle, within the limitations of the feature sizes achievable with deep reactive ion etching (DRIE) microfabrication, subject to our need to demold the resulting scaffold without tearing. We hypothesis that a hybrid approach between traditional compliant mechanism–based design (*40*) and numerical geometry optimization techniques (*64*) would yield the best results for any future biohybrid systems seeking to implement a compliant mechanism.

Specific to the case of flagellate-type biohybrid robots, we propose additional considerations. In this design, we have not explored alternative placements for the tails. In a fully compliant mechanism, there can be unexpected locations on the boundary that undergo large angular deflection, and the tails could be placed at these locations. Likewise, the offset angle can be adjusted on the basis of the expected tonic force in the muscle on DIV 10. Further, the tails do not necessarily need to be straight or the same cross section along their entire length. In addition, in this intermediate-*Re* regime, there is no reason to expect the optimal speed of the swimmer to still correspond to an *Sp* of 2.1. These considerations are potentially valuable avenues for theoretical and experiment exploration.

Adaptability of the muscle to attachment stiffness

Because our swimmer design requires sacrificial supports to aid in mounting the muscle ring on the grips, we investigated the effect of changing mechanical stiffness on the muscle development. The need for sacrificial supports is a common feature in the design of microscale biohybrid swimmers and walkers that use 3D tissues (*12*, *65*, *66*). This is because the scale of the systems makes direct manipulation difficult and things such as sacrificial supports and sacrificial molds aid in manipulation.

We argue that a key advantage of muscle-based actuators is their ability to function in untethered, microscale devices. The difficulty associated with porting a battery to power a motor on a microscale robot is one of the key motivating factors driving researchers to combining optogenetics and biological actuators (*16*). Although the modular nature of muscle makes it suitable for untethered actuators, forming muscle tissues in situ at small scale is often difficult. Seeding muscle rings in separate tissue molds and transferring them onto the bioactuator scaffold after tissue formation, as we have done in this work, is a feasible alternative to in situ tissue formation (*8*, *17*).

We propose that the robustness of muscle to mechanical perturbation may allow for more flexibility in the design of biohybrid robots. The effect of time-varying mechanical stiffness on the development of skeletal muscle has not been investigated previously. There are studies that look at muscle development on scaffolds of different linear stiffness but not with a time-varying perturbation element. Our results suggest that C2C12-derived muscles grown against anchors with mechanical stiffness on the order of 0.1 to 1 μN/μm do not strongly vary their target tonic tension in response to variations or perturbations in mechanical stiffness within this range (Fig. 4E). This result adds to our knowledge of tonic tension in myogenesis, and it may permit the design of biohybrid robots that change configuration, and likely therefore mechanical anchor stiffness, during their development, opening the possibility of new ways to circumvent the need for sacrificial supports or to allow for their strategic and convenient placement.

We can consider the consistency of this finding with previous studies that measured the tonic tension in muscle tissues. We found that the tension increased up to DIV 11 before leveling off (Fig. 4E). A comparable result was observed in Powell *et al.* (*67*) with tissue-engineered human skeletal muscle. Between DIV 9 and 14 after seeding their muscles, researchers applied a constant stretch to the muscle, increasing it by 5% every 2 days. Even with this mechanical perturbation, the tonic tension in the muscle stayed in the range of 400 to 600 μN. This is similar to the tonic tension found in our muscles, and, by coincidence, our muscle rings and their tissues have similar cross-sectional areas of ~1 mm^2. In their case, applying a constant stretch has the effect of transiently increasing the tonic force in the muscle. The muscle tension was observed to relax back to a homeostatic value. In our case, the muscles rebuilt their tonic tension after drops in tension and changes in anchor stiffness.

Our experiments do not indicate how mechanical stiffness will affect other aspects of muscle development aside from tonic force. A comparison between muscle development on soft and stiff pillars has been performed before in the context of training in vitro muscle constructs with electrical stimulation (*68*). It was found that the benefits of training with electrical stimulation depended on the anchor stiffness. On a soft pillar, the training leads to increased contractility, but on a stiff pillar, training over multiple days had no improvement over stimulating the muscle for 1 hour the same day that contractility is measured. So, although tonic forces may be comparable for different stiffnesses, the performance of the muscle and its response to other cues may vary with stiffness. In addition, it has been found that muscles cocultured with motor neurons exhibit hypertrophy from chronic electrical stimulation, while muscle tissues by themselves do not (*69*). We therefore suspect that the performance of skeletal muscle and its response to training will depend on anchor stiffness and whether it is cocultured with motor neurons. Such an investigation would benefit from granular tunability of the spring stiffness and traditional measures of muscle maturity including mRNA markers (*69*), sarcomere numbers, and ECM composition (*70*).

Effect of motor neurons on muscle performance

The coculture of muscle with motor neurons has been shown to improve the development of sarcomeric structures in the muscle (*31*), perhaps due to chemical cross-talk that leads to the secretion of growth factors, which support muscle development and neural connectivity (*50*, *51*). Our results showed that muscles grown in coculture with motor neurons demonstrate fourfold higher contractility compared to muscles grown by themselves (Fig. 5E). We also observed that cocultured muscles were more likely to be twitching spontaneously on DIV 10. This improvement in contractility and increase in spontaneous twitching occurred within 2 days of the introduction of motor neurons to the coculture, which studies suggest is too early for functional NMJ formation between the muscle and the neurons, which typically takes 3 to 5 days (*12*, *71*, *72*). Previous studies have shown that spontaneous twitching plays a role in the formation of organized sarcomeres inside of muscle fibers (*42*). Studies have also shown an increase in spontaneous electrical activity and the release of acetylcholine when motor neurites contact muscle fibers in vitro before the formation of mature synapses (*73*).

On our swimmers, the neurites were able to sense and grow toward the muscles (Fig. 3G), which may have been due to their proximity and the presence of a physical bridge of ECM between them. We hypothesize that the improvement in the muscle contractility depends on this ability for the neurons to sense the muscle and that it is the result of bidirectional cross-talk. Because our swimmer platform is untethered and not designed for complex imaging, it is ill suited for deeper study into the cross-talk between cocultured muscle and motor neurons. However, our fabrication technique for the ECM bridges that connect the muscle to the motor neurons may lend itself to new coculture platforms. Existing microfluidic culture systems for NMJs involve a muscle formed on compliant pillars for reading out force, connected to a stationary population of motor neurons (*31*, *34*, *74*). However, with a variation on this technique, it would be possible to create free-standing bridges of ECM between tissues, allowing for more flexibility with the placement of muscle and neurons.

Inertia in swimmer propulsion and flow regime transition

Our design for a fast flagellate-type swimmer was premised on simulations of low-*Re* theory (*39*). With our initial, nonoptimized design (Fig. 2), we had not predicted more than a 10-fold increase in swimming speed over previous biohybrid flagellate swimmers, but we had expected consistency with low-*Re* theory. The observed 100-fold increase suggests a transition to an intermediate-*Re* flow regime and a different mechanism of propulsion from low-*Re* swimming (Fig. 8A). Further evidence for this change in flow regime comes from the observation of persistent motion of the swimmer (Fig. 7F). Our swimmers operate between *Re* ~ 0.01 and 1. On the basis of this change in flow regime, we ascribe our swimmer dynamics to an intermediate-*Re* regime. Our particle streak imaging investigation of this transition showed a change in particle dynamics consistent with our experimental swimming results (Fig. 9F). These experiments also showed a dependence of the flow regime on the muscle contraction velocity, which was not possible to modulate in the experiments with the biohybrid swimmers.

Swimming at intermediate *Re* has been examined theoretically in the literature for some special cases (*22*, *36*, *37*, *75*). Researchers have looked at the speed of a swimmer with respect to its flapping Reynolds number $Re_\mathrm{f} = \rho_\mathrm{body} A\omega L / \mu$, calculated from the frequency ω and amplitude *A* of actuation and the body density ρ_body. Theoretical studies predict swimming speed proportional to $\left(Re_\mathrm{f}\right)^\alpha$ for dense swimmers, where the swimmer density is much higher than the fluid density, and for swimmers near asymmetric boundaries. In both cases, the introduction of inertia to the propulsion is continuous with increasing *Re*. The applicable case to our swimmer is one where the swimmer density is similar to the surrounding fluid. The general case of this has not been investigated theoretically (*37*). However, an analysis was performed for the specific case of a dimer swimmer by linearizing the Navier-Stoke's equations around *Re* ~ 1 (*76*). This analysis has not been extended to the case of a 2D flagellate.

A few biological swimmers have a similar size scale to that of our swimmer, including newborn tadpoles, which operate at a higher $Re \sim 10^2$ to 10^4 (*77*), and mosquito larvae (*78*). A species of sea slug called *Clione antarctica* exhibits both nonreciprocal low-*Re* and reciprocal high-*Re* locomotion. Studies looking at the transition between the two swimming regimes have found that inertial propulsion would arise discontinuously when the amplitude and frequency of the flapping of the slug's "wings" exceeded a threshold (*79*). They attributed it to a transition through a hydrodynamic instability. They computed this threshold with respect to the unsteady Reynolds number $Re_\omega = \rho_\mathrm{body} \omega L^2 / \mu$, which is calculated on the basis of the frequency of flapping ω, the density of the body ρ_body, and the length scale of the body *L*. It is a measure of how quickly the sea slug flaps its wings. They found that the threshold lies between $Re_\omega \sim 5$ to 20, which may be specific to this sea slug. The corresponding value for our swimmer increases with grip velocity. Our quantification of the flow transition based on the bead velocities suggests a gradual transition around a critical grip velocity around 460 μm/s, above which bead velocity depends strongly on tail angular displacement (Fig. 9E). Our results from particle streak imaging show the potential for an even faster swimmer at the same or a smaller size scale by increasing the angular displacement and velocity of the tails. As a biological motivation for this, we note that newborn tadpoles are able to swim at velocities in the millimeters per second to centimeters per second range despite only being 5 to 10 mm long (*Re* ~ 100).

We studied the design of muscle-powered biohybrid robots and the biomimetic small-scale locomotion of low- to intermediate-*Re* swimming. On the basis of analytical models of low-*Re* swimming, we pursued the fabrication of a muscle-powered biohybrid swimmer. We wanted to see whether simulations showing improvement in thrust with increasing tail angular actuation could be validated. Our mechanical design centered around a compliant linkage to convert linear muscle contraction to angular displacement. (i) We found that the geometry of a compliant linkage interfaced with biological tissue presents a multifacetted optimization problem subject to the limitations of the fabrication technology. To integrate the muscle, we introduced sacrificial structural elements, which also acted to disrupt the stiffness of the muscle mechanical anchorage. (ii) In working with this design, we found that the muscle would tend toward a homeostatic tonic tension irrespective of perturbation in the mechanical anchorage stiffness. To support muscle maturation, we tried introducing motor neurons capable of sensing and growing toward the muscle, and (iii) we found a fourfold improvement in muscle contractility. These results have implications for the biophysics of myogenesis and the design of future biohybrid robots. (iv) Swimming experiments showed evidence of the involvement of inertia in the swimming dynamics indicating a transition from a low- to intermediate-*Re* flow regime. A study of the flow field confirmed this result. We found that at the tail angular displacements and muscle contraction velocities exhibited by our swimmers, the velocity of the flow undergoes a gradual transition, which depends on the angular velocity of the tail. A better understanding of the scaling laws of this flow regime may allow for a class of fast, intermediate-*Re*, microscale biohybrid swimmers.

MATERIALS AND METHODS

Swimmer scaffold fabrication and calibration

The swimmer scaffold is molded from PDMS (Dow Corning Sylgard 184, 10:1 base to cross-linker ratio) at 60°C for 2 days using a microfabricated silicon mold for the head and tails and a 3D-printed resin mold for the neuron holder. The silicon wafer was patterned using standard photolithography procedures and etched to a depth of 155 μm using DRIE based on the Bosch-process in an STS Pegasus inductively coupled plasma tool. The wafer was then coated with PTFE, which acts as a release agent that helps with the demolding of PDMS. The resin mold was printed from Clear V4 resin in a Form3 SLA 3D printer (Formlabs) with a minimum feature size of around 200 μm. The two components are manually assembled with liquid PDMS and cured at 60°C for 2 days. The assembled swimmer scaffold is autoclaved in distilled water to drive out monomers and then autoclaved again with a dry cycle to sterilize.

We take the characteristic length of the swimmer scaffold to be 9 mm based on the distance from the head of the swimmer to the ends of the tails in the direction of swimmer. We calculate the maximum sperm number Sp of the swimmer to be 1.4 based on the dimensions of the tail and a maximum stimulation frequency for the muscle of 5 Hz before it starts to experience tetanus. Sp is given by $Sp = L\left(\frac{\omega\xi_{\perp}}{A}\right)^{1/4}$, where L is the tail length, ω is the angular actuation frequency, A is the flexural rigidity, and $\xi_{\perp}$ is the drag coefficient of the tail per unit length normal to its length. The tail length is 5.8 mm. The flexural rigidity is the product of the Young's modulus of the PDMS estimated as 1.9 MPa and the second moment of area of the 155-μm-deep and 100-μm-wide tail, given by $I = \frac{w^3 b}{12}$, where w is the width and b is the depth. The effective radius of the tail cross section is the radius of a circle with the same cross-sectional area, $r = \sqrt{(wb)}$. The drag coefficient for this aspect ratio of the length of the tail to its effective radius, $L / r \approx 90$, requires a correction factor in the calculation of $\xi_{\perp}$ from resistive force theory, $\xi_{\perp} = \frac{4\pi\mu}{\log(L/r)} + 0.193$ (*45*).

The force-displacement relationship at the grips of the scaffold is calibrated in water with respect to a tungsten needle of known length and diameter (Living Systems Instrumentation; Young's modulus, 411 GPa; stiffness, 0.43 μN/μm). During calibration, the scaffold is adhered to a dish with double-sided tape at the edge of where the neuron holder sits.

Skeletal muscle ring fabrication and mounting

C2C12 muscle rings were fabricated and cultured following standard protocols (*17*, *80*). Briefly, C2C12 mouse myoblasts (American Type Culture Collection, catalog no. CRL-1772) were thawed from cryogenic storage and resuspended in growth medium consisting of DMEM, supplemented with 10% (v/v) fetal bovine serum (FBS), 1× GlutaMAX, and 1× penicillin/streptomycin (all reagents purchased from Gibco, Thermo Fisher Scientific). Cells were then plated at a density of 2×10^4 cells/cm^2 in a T75 culture flask. The growth medium was changed every other day, and the cells were passaged once they reached 50 to 70% confluency. All C2C12 cells used in this study were at passage 5.

Annulus-shaped ring molds with an inner diameter of 3 mm were fabricated from PDMS using SLA-printed resin negatives. To prevent cell adhesion, the ring molds were incubated in a 1% (w/v) Pluronic solution (Sigma-Aldrich, Pluronic F-127; reconstituted from powder and filtered through 0.22 μm pores) at 20°C overnight. Afterward, the solution was removed, and the ring molds were rinsed three times with saline.

A C2C12-ECM mixture was prepared containing 2.5×10^6 cells/ml, type I rat tail collagen (2 mg/ml; Corning, catalog no. 354249), and Matrigel (2 mg/ml; Corning, catalog no. 356231). The collagen stock solution was neutralized with a 7% sodium bicarbonate solution and 10× minimum essential medium. Muscle rings were cast using 70 μl of cell-ECM mixture and cured at 37°C for 45 min. The mold was then inundated in growth medium. The day when the muscle rings are seeded is DIV 0. The rings were left to compact until DIV 2. The compaction ratio was around 10:1, resulting in rings with a cross section of 1 mm by 0.5 mm and an inner diameter of 3 mm (Fig. 3B).

On DIV 2, the rings were mounted on the swimmer scaffold (Fig. 3C). Briefly, the swimmer scaffold was fixed to a block of PDMS using insect pins and placed under a stereo microscope. The scaffold was inundated with growth medium, and the ring was added to the dish. Using two pairs of tweezers, the grips of the scaffold were opened, and the ring was placed inside. Then, the medium was changed in all dishes to reduce the risk of contamination. The rings were maintained in low-serum differentiation medium [DMEM supplemented with 2% (v/v) horse serum, 1× GlutaMAX, 1× penicillin/streptomycin, and 1× ITS supplement; all reagents from Gibco] until DIV 18 or until motor neurons were added on DIV 8. The muscles tend to start responding to electrical stimulation on DIV 6 (monophasic, 10-ms pulse width, and field strength of 3 V/cm).

The sacrificial supports connecting the grips to the head of the swimmer were removed using surgical scissors under a stereo microscope. The scissors cutting into the PDMS causes the grips to twist. The muscle rings tend to survive this step because they can flex along with the grips. Once the supports are cut, tonic tension in the muscle rings may cause one of the grips to twist out of plane.

Preparation and seeding of the motor neuron spheroids

The procedure for preparation of motor neuron spheroids from optogenetic mESCs (line ChR2^{H134R}-HBG3 Hb9-GFP) is described elsewhere (*12*, *34*). The procedure for adding these spheroids to the swimmer is shown in Fig. 3D. The swimmers were removed from their mounting pedestals and placed on a parafilm sheet with a 100-μl droplet of medium. Spheroids were mixed with the same reconstituted mixture of collagen and Matrigel as described above. The droplet of medium was entirely removed from around the swimmer, and the spheroid-ECM mixture was injected into the neuron holder on the head of the swimmer. An additional 20 μl of ECM was dispensed around the head of the swimmer and the muscle to protect it from dehydration and to form a continuous bridge of ECM from the muscle to the neurospheres. The ECM was cured at 37°C and 100% humidity for 30 min. Next, the swimmers were pinned back onto their mounting pedestals and inundated with coculture medium [47% (v/v) Neurobasal Plus medium, 47% (v/v) advanced DMEM/F-12, 2% (v/v) FBS, 1× GlutaMAX, 1× penicillin/streptomycin, 1× B-27 Plus supplement, 1× ITS supplement, and 0.1 mM β-mercaptoethanol; all reagents from Gibco]. Upon inundation, loose ECM fragments tended to dislodge, but the ECM surrounding the neurospheres and in the narrow space between the muscle and the head of the swimmer tended to remain intact, forming a bridge. This ECM bridge frequently survived inundation when the sacrificial supports were still intact. Coculture medium was refreshed every other day for the remainder of the experiment.

Electric field stimulation and recordings of swimmers

Typically, for voltages exceeding 1.5 V, electrolysis will cause bubbles to form at the electrodes and the pH of the medium to shift. However, at sufficiently short pulse widths, bubbles do not appear to form, and the pH remains stable. In this study, we used a maximum pulse width of 10 ms. Aside from keeping the biological components healthy, this is important because the formation of bubbles can induce flow in the dish that causes the swimmer to drift. The strength of electrical stimulation is controlled by fixing the voltage across a pair of electrodes, which we report normalized to the distance between the electrodes. During a stimulation pulse, electric current passes through the medium and through the muscle, initiating a contraction. The voltage drop felt across a particular muscle will vary on the basis of its impedance and its orientation to the electrodes. In this study, we disregard these potential sources of variability.

Electric field stimulation (monophasic and 10-ms pulse width) was applied using a pair of graphite electrodes, 20 mm by 20 mm by 3 mm, positioned on either side of the swimmer. The resulting evoked muscle contractions were imaged using an inverted microscope (Olympus IX81) with a 2× air objective and recorded at up to 100 frames/s using a digital complementary metal-oxide semiconductor camera (Hamamatsu ORCA-Flash4.0 V3). To evaluate swimming performance, the swimmer was placed in a 100-mm-diameter polystyrene dish (Thermo Fisher Scientific, BioLite) containing 30 ml of coculture medium and 10 ml of Percoll (Sigma-Aldrich). The higher density of Percoll causes it to settle to the bottom of the dish, resulting in a distinct interface between the Percoll and the cell culture medium (fig. S3A). The swimmer was submerged in the dish and was observed to float in the Percoll gradient several millimeters above the bottom of the dish. The graphite electrodes were placed 4 cm apart so that the swimmer was at least a body length away from either electrode. In addition to microscopy imaging, recordings were also taken with a Canon Rebel Ti camera (29.97 frames/s), which allowed for tracking the swimmer over a larger field of view.

Image processing and analysis of swimming

Tracking of the head of the swimmer was performed using the template matching plugin in ImageJ. Swimming displacement was quantified by projecting the motion of the swimmer onto its time-averaged swimming trajectory. For a given test, the trajectory may vary with time to account for rigid body rotation of the swimmer, which can result from asymmetric thrust generation by the tails. Once the overall motion of the swimmer has been subtracted, the displacements of the grips were tracked at x_3 where the grips meet the coupler. The calibration of the swimmer reported in Fig. 2 was used to approximate the displacement of the grips at x_4. From this, the muscle-driven grip velocity was approximated.

Low *Re* elastohydrodynamic model simulations

The full details of the elastohydrodynamic model simulated in this paper appear in Aydin *et al.* (*39*), and the relevant MATLAB codes are made available (https://github.com/wdrennan/Biohybrid-Swimmer-Digital-Assets). A second-order-accurate, implicit finite difference method is used for simulating the filament dynamics. The simulation takes the heave (x_2, δ) and twist ($\Delta\theta$) of the tails as boundary conditions. These are calculated on the basis of the grip movement at x_3 for the test shown in Fig. 7 using the calibrations shown in Fig. 2E. When simulating the swimming speed for a wider range of angles in Fig. 8A, the $x_3(t)$ waveform for a given frequency is scaled so that the amplitude corresponds with the appropriate twist angle change using these same calibrations. The simulations were run using the experimentally derived drag coefficient ($\gamma = 9.6$ mg/s) and the predicted drag coefficient ($\gamma = 42.6$ mg/s). As a note, in the low-*Re* model, the thrust depends on the drag asymmetry of the tails, $\zeta_{\perp} - \zeta_{\parallel}$. The experimentally derived drag coefficient ($\gamma = 9.6$ mg/s) is smaller than that calculated for the tails ($\gamma = 21.6$ mg/s). This experimentally derived drag coefficient contradicts our calculated value of $\zeta_{\perp}$ and $\zeta_{\parallel}$. In the low-*Re* model, we use the predicted values of $\zeta_{\perp}$ and $\zeta_{\parallel}$ to compute the thrust, even when this constitutes a contradiction with the experimental drag coefficient. We assume a PDMS stiffness of 1.9 MPa and use the dimensions of our swimmer's tail cross section of 100 μm wide and 155 μm deep (*13*).

Particle streak imaging of swimmer tail flow field using a programmable micromanipulator

A swimmer scaffold was affixed with tape to the middle of a petri dish, such that it is positioned 2 mm above the floor of the dish. The dish was filled with saline. A mixture of Percoll (5 ml) and 15.45-μm-diameter polystyrene beads (Bangs Laboratories Inc., catalog no. PS07002) was pipetted near the edge of the dish. The Percoll displaced the saline and spread across the floor of the dish along with the polystyrene beads. Buoyancy causes the beads to float to the Percoll-saline interface. A three-axis micrometer stage affixed with a stepper motor was placed next to the dish. A hypodermic needle attached to the end effector of the stage was lowered into the grip of the swimmer scaffold. An Arduino Uno was used to control the motion of the hypodermic needle. The needle was programmed to follow a symmetric trapezoidal waveform with constant speed, a 0.1-s dwell at maximum displacement, and a dwell time of 1.1 s between subsequent cycles. This dwell time was introduced to allow the beads to settle after each cycle, uncoupling them from one another.

The tracer particles were found suitable for this application based on their Stokes number. The Stokes number is calculated as a ratio between the response time of the particles and the characteristic time constant of the flow. The response time can be calculated with the formula $\tau_p = d_p^2 \frac{\rho_p}{18\mu}$ where d_p is the particle diameter, ρ_p is the particle density, and μ is the kinematic viscosity of the fluid (*63*). The characteristic time constant of the flow can be calculated from the characteristic velocity of the flow and a characteristic length. For an upper bound, we take the characteristic velocity as the maximum tip velocity of the swimmer tail at the highest grip speed, which is ~20 mm/s. We take the characteristic length as the thickness of the tail, 100 μm. We find that the Stokes number is $\sim 3 \times 10^{-3}$, well below the rule of thumb maximum value of 0.1 for tracer particles.

Particle streak images were made by taking recordings of the tracer particles at 100 frames/s. By inverting the pixel intensity values of the images and producing a maximum intensity z-projection through the image stack, we end up with images showing the extent of the motion of the swimmer tail and the paths of each of the particles. We verified that these are the paths traced by the beads using an ImageJ template matching plugin to track some of the beads.

Each tests involved a fixed grip speed and a fixed maximum tail angular displacement amplitude. After each test, we formed a composite image using the steak image as well as the first and last images in each recording, thresholded to only see the beads as dots. The composite images show the paths of the particles with a red dot at the initial position of each particle and a blue dot at the final position of each particle. Some bleed through from the thresholding processes leaves blue and red artifacts in the images, which are easily distinguishable as such. We labeled each of the images with the corresponding grip speed and tail angular displacement and assembled a lossless, uncompressed video of the images (movie S5).

We can find the net displacement of each bead by following it from its starting position (red) to its ending position (blue). We project the displacement vector of the bead along the tail. To calculate the time-average speed, we divide this distance by the duration it takes for the tail to complete 5 cycles for a given fixed grip speed and maximum tail angular displacement, including dwell time.

Immunostaining of the muscle rings

For immunofluorescence imaging, samples were fixed in 4% (v/v) paraformaldehyde in phosphate-buffered saline (PBS) overnight at 4°C. The samples were then permeabilized using 0.2% (v/v) Triton X-100 in PBS and blocked with a solution of 3% (w/v) bovine serum albumin and 5% (v/v) normal goat serum in PBS. Following this, the samples were incubated overnight at 4°C with a rabbit anti–α-actinin primary antibody (1:250; Abcam, catalog no. ab68167). After washing the samples five times with PBS (5 min per wash), they were incubated with goat anti-rabbit secondary antibody conjugated with Alexa Fluor 568 (1:1000; Abcam, catalog no. ab175695) overnight at 4°C. The next day, samples were washed three times with PBS and incubated with 4′,6-diamidino-2-phenylindole (1:1000; Invitrogen) for 10 min, followed by another three washes in PBS. Images were acquired using a Zeiss LSM 700 confocal microscope equipped with an EC Plan-Neofluar 20×/0.5 numerical aperture objective (Carl Zeiss AG).

Statistical methods

A series of three–independent sample, weighted, one-way analysis of variance (ANOVA) tests was used to compare the force and length of the aneural swimmer in each of the three sample populations on each day (Fig. 4, D and E). On days where the sacrificial supports were cut, the force and length values measured after cutting were used. P values are used to reject the null hypothesis that all the swimmer samples come from the sample population. A series of Student's two-tailed t tests assuming independent samples was used to compare the spontaneous and evoked contractility of aneural and cocultured swimmer samples (Fig. 5B). The behavior of a swimmer during inertial drift was characterized by least-squares curve fitting with the given exponential function with affine offset (Fig. 7F). The value for v_{drift} is taken by fitting a linear function to the projected swimmer position over time before stimulation began. R^2 values are presented as means ± SEM for the given groupings.

Supplementary Materials

The PDF file includes:

Figs. S1 to S3

Legends for movies S1 to S5

Other Supplementary Material for this manuscript includes the following:

Movies S1 to S5

REFERENCES AND NOTES

1. V. A. Webster-Wood, "It's alive! From bioinspired to biohybrid robots," in *Robotics in Natural Settings. CLAWAR 2022. Lecture Notes in Networks and Systems*, J. M. Cascalho, M. O. Tokhi, M. F. Silva, A. Mendes, K. Goher, M. Funk, Eds. (Springer, 2023), vol. 530, pp. 4.
2. R. Desatnik, Z. J. Patterson, P. I. Gorzelak, S. I. Zamora, P. LeDuc, C. Majidi, Soft robotics informs how an early echinoderm moved. *Proc. Natl. Acad. Sci. U.S.A.* **120**, e2306580120 (2023).
3. R. Mestre, T. Patiño, S. Sánchez, Biohybrid robotics: From the nanoscale to the macroscale. *Wiley Interdiscip. Rev. Nanomed. Nanobiotechnol.* **13**, e1703 (2021).
4. M. Filippi, O. Yasa, J. Giachino, R. Graf, A. Balciunaite, L. Stefani, R. K. Katzschmann, Perfusable biohybrid designs for bioprinted skeletal muscle tissue. *Adv. Healthc. Mater.* **12**, 2300151 (2023).
5. M. Filippi, M. Mekkattu, R. K. Katzschmann, Sustainable biofabrication: From bioprinting to AI-driven predictive methods. *Trends Biotechnol.* **43**, 290–303 (2025).
6. V. A. Webster-Wood, O. Akkus, U. A. Gurkan, H. J. Chiel, R. D. Quinn, Organismal engineering: Towards a robotic taxonomic key for devices using organic materials. *Sci. Robot* **2**, eaap9281 (2017).
7. V. A. Webster-Wood, M. Guix, N. W. Xu, B. Behkam, H. Sato, D. Sarkar, S. Sanchez, M. Shimizu, K. K. Parker, Biohybrid robots: Recent progress, challenges, and perspectives. *Bioinspir. Biomim.* **18**, 015001 (2023).
8. M. Guix, R. Mestre, T. Patiño, M. De Corato, J. Fuentes, G. Zarpellon, S. Sánchez, Biohybrid soft robots with self-stimulating skeletons. *Sci. Robot* **6**, eabe7577 (2021).
9. J. C. Nawroth, H. Lee, A. W. Feinberg, C. M. Ripplinger, M. L. McCain, A. Grosberg, J. O. Dabiri, K. K. Parker, A tissue-engineered jellyfish with biomimetic propulsion. *Nat. Biotechnol.* **30**, 792–797 (2012).
10. A. Balciunaite, O. Yasa, M. Filippi, M. Y. Michelis, R. K. Katzschmann, "Bilayered biofabrication unlocks the potential of skeletal muscle for biohybrid soft robots," in *2024 IEEE 7th International Conference on Soft Robotics, RoboSoft 2024* (Institute of Electrical and Electronics Engineers Inc., 2024), pp. 525–530.
11. S. J. Park, M. Gazzola, K. S. Park, S. Park, V. Di Santo, E. L. Blevins, J. U. Lind, P. H. Campbell, S. Dauth, A. K. Capulli, F. S. Pasqualini, S. Ahn, A. Cho, H. Yuan, B. M. Maoz, R. Vijaykumar, J. W. Choi, K. Deisseroth, G. V. Lauder, L. Mahadevan, K. K. Parker, Phototactic guidance of a tissue-engineered soft-robotic ray. *Science* **353**, 158–162 (2016).
12. O. Aydin, X. Zhang, S. Nuethong, G. J. Pagan-Diaz, R. Bashir, M. Gazzola, M. T. A. Saif, Neuromuscular actuation of biohybrid motile bots. *Proc. Natl. Acad. Sci. U.S.A.* **116**, 19841–19847 (2019).
13. B. J. Williams, S. V. Anand, J. Rajagopalan, M. T. A. Saif, A self-propelled biohybrid swimmer at low Reynolds number. *Nat. Commun.* **5**, 3081 (2014).
14. R. Mestre, J. Fuentes, L. Lefaix, J. Wang, M. Guix, G. Murillo, R. Bashir, S. Sánchez, Improved performance of biohybrid muscle-based bio-bots doped with piezoelectric boron nitride nanotubes. *Adv. Mater. Technol.* **8**, 2200505 (2023).
15. J. Wang, X. Zhang, J. Park, I. Park, E. Kilicarslan, Y. Kim, Z. Dou, R. Bashir, M. Gazzola, Computationally assisted design and selection of maneuverable biological walking machines. *Adv. Intell. Syst.* **3**, 2000237 (2021).
16. Y. Kim, Y. Yang, X. Zhang, Z. Li, A. Vázquez-Guardado, I. Park, J. Wang, A. I. Efimov, Z. Dou, Y. Wang, J. Park, H. Luan, X. Ni, Y. Seong Kim, J. Baek, J. Jaehyung Park, Z. Xie, H. Zhao, M. Gazzola, J. A. Rogers, R. Bashir, Remote control of muscle-driven miniature robots with battery-free wireless optoelectronics. *Sci. Robot.* **8**, eadd1053 (2023).
17. Z. Li, Y. Seo, O. Aydin, M. Elhebeary, R. D. Kamm, H. Kong, M. T. A. Saif, Biohybrid valveless pump-bot powered by engineered skeletal muscle. *Proc. Natl. Acad. Sci. U.S.A.* **116**, 1543–1548 (2019).
18. Y. Morimoto, H. Onoe, S. Takeuchi, Biohybrid robot powered by an antagonistic pair of skeletal muscle tissues. *Sci Robot* **3**, eaat4440 (2018).
19. Y. Morimoto, H. Onoe, S. Takeuchi, Biohybrid robot with skeletal muscle tissue covered with a collagen structure for moving in air. *APL Bioeng.* **4**, 026101 (2020).
20. Y. Akiyama, T. Sakuma, K. Funakoshi, T. Hoshino, K. Iwabuchi, K. Morishima, Atmospheric-operable bioactuator powered by insect muscle packaged with medium. *Lab Chip* **13**, 4870–4880 (2013).
21. E. M. Purcell, Life at low Reynolds number. *Am. J. Phys.* **45**, 3–11 (1977).
22. E. Lauga, Life around the scallop theorem. *Soft Matter* **7**, 3060–3065 (2011).
23. F. Jabr, How to swim in molasses. *Sci. Am.* **309**, 90–95 (2013).
24. F. B. Tian, L. Wang, Numerical modeling of sperm swimming. *Fluids* **6**, 73 (2021).
25. D. Y. Tiioe, S. Oentoeng, The viscosity of human semen and the percentage of motile spermatozoa. *Fertil. Steril.* **19**, 562–565 (1968).

26. H. M. Hübner, R. Heidl, W. Krause, Investigation of flow behaviour (viscosity) from human seminal fluid with a rotational viscosimeter. *Andrologia* **17**, 592–597 (1985).
27. J. L. Simpson, S. Humphries, J. P. Evans, L. W. Simmons, J. L. Fitzpatrick, Relationships between sperm length and speed differ among three internally and three externally fertilizing species. *Evolution* **68**, 92–104 (2014).
28. J. L. Fitzpatrick, F. Garcia-Gonzalez, J. P. Evans, Linking sperm length and velocity: The importance of intramale variation. *Biol. Lett.* **6**, 797–799 (2010).
29. M. Shin, T. Ha, J. Lim, J. An, G. Beak, J. H. Choi, A. A. Melvin, J. Yoon, J. W. Choi, Human motor system-based biohybrid robot-on-a-chip for drug evaluation of neurodegenerative disease. *Adv. Sci.* **11**, e2305371 (2024).
30. J. Andersen, O. Revah, Y. Miura, N. Thom, N. D. Amin, K. W. Kelley, M. Singh, X. Chen, M. V. Thete, E. M. Walczak, H. Vogel, H. C. Fan, S. P. Paşca, Generation of functional human 3D cortico-motor assembloids. *Cell* **183**, 1913–1929.e26 (2020).
31. O. Aydin, A. P. Passaro, M. Elhebeary, G. J. Pagan-Diaz, A. Fan, S. Nuethong, R. Bashir, S. L. Stice, M. T. A. Saif, Development of 3D neuromuscular bioactuators. *APL Bioeng.* **4**, 016107 (2020).
32. M. A. Bakooshli, E. S. Lippmann, B. Mulcahy, N. Iyer, C. T. Nguyen, K. Tung, B. A. Stewart, H. Van Den Dorpel, T. Fuehrmann, M. Shoichet, A. Bigot, E. Pegoraro, H. Ahn, H. Ginsberg, M. Zhen, R. S. Ashton, P. M. Gilbert, A 3D culture model of innervated human skeletal muscle enables studies of the adult neuromuscular junction. *eLife* **8**, e44530 (2019).
33. A. Natarajan, A. Sethumadhavan, U. M. Krishnan, Toward building the neuromuscular junction: In vitro models to study synaptogenesis and neurodegeneration. *ACS Omega* **4**, 12969–12977 (2019).
34. S. G. M. Uzel, R. J. Platt, V. Subramanian, T. M. Pearl, C. J. Rowlands, V. Chan, L. A. Boyer, P. T. C. So, R. D. Kamm, Microfluidic device for the formation of optically excitable, three-dimensional, compartmentalized motor units. *Sci. Adv.* **2**, e1501429 (2016).
35. Y. Morimoto, M. Kato-Negishi, H. Onoe, S. Takeuchi, Three-dimensional neuron-muscle constructs with neuromuscular junctions. *Biomaterials* **34**, 9413–9419 (2013).
36. E. Lauga, Continuous breakdown of Purcell's scallop theorem with inertia. *Phys. Fluids* **19**, 061703 (2007).
37. D. Gonzalez-Rodriguez, E. Lauga, Reciprocal locomotion of dense swimmers in Stokes flow. *J. Phys. Condens. Matter* **21**, 204103 (2009).
38. T. S. Yu, E. Lauga, A. E. Hosoi, Experimental investigations of elastic tail propulsion at low Reynolds number. *Phys. Fluids* **18**, 091701 (2006).
39. O. Aydin, K. Hirashima, M. T. A. Saif, Incorporating geometric nonlinearity in theoretical modeling of muscle-powered soft robotic bio-actuators. *J. Appl. Mech.* **91**, 011008 (2024).
40. L. L. Howell, *Compliant Mechanisms* (John Wiley & Sons, 2001).
41. J. Chal, O. Pourquié, Making muscle: Skeletal myogenesis in vivo and in vitro. *Development* **144**, 2104–2122 (2017).
42. M. Weitkunat, M. Brasse, A. R. Bausch, F. Schnorrer, Mechanical tension and spontaneous muscle twitching precede the formation of cross-striated muscle in vivo. *Development* **144**, 1261–1272 (2017).
43. J.-S. Kang, P. J. Mulieri, C. Miller, D. A. Sassoon, R. S. Krauss, CDO, A robo-related cell surface protein that mediates myogenic differentiation. *J. Cell Biol.* **143**, 403–413 (1998).
44. E. N. Olson, Interplay between proliferation and differentiation within the myogenic lineage. *Dev. Biol.* **154**, 261–272 (1992).
45. R. G. Cox, The motion of long slender bodies in a viscous fluid Part 1. General theory. *J. Fluid Mech.* **44**, 791–810 (1970).
46. I. Eames, C. A. Klettner, Stokes' and Lamb's viscous drag laws. *Eur. J. Phys.* **38**, 025003 (2017).
47. B. Emon, Z. Li, S. H. Joy, U. Doha, F. Kosari, M. T. A. Saif, A novel method for sensor-based quantification of single/multicellular force dynamics and stiffening in 3D matrices. *Sci. Adv.* **7**, eabf2629 (2021).
48. G. K. Toworfe, R. J. Composto, C. S. Adams, I. M. Shapiro, P. Ducheyne, M. T. A. Saif, "Effect of surface activated poly(dimethylsiloxane) on fibronectin adsorption and cell function," in *Mat. Res. Soc. Symp. Proc.* Vol. EXS-1, 2004, pp. F7.8.1-F7.8.5.
49. G. Agrawal, A. Aung, S. Varghese, Skeletal muscle-on-a-chip: An in vitro model to evaluate tissue formation and injury. *Lab Chip* **17**, 3447–3461 (2017).
50. J. Saini, A. Faroni, A. J. Reid, V. Mouly, G. Butler-Browne, A. P. Lightfoot, J. S. McPhee, H. Degens, N. Al-Shanti, Cross-talk between motor neurons and myotubes via endogenously secreted neural and muscular growth factors. *Physiol. Rep.* **9**, e14791 (2021).
51. K. Y. Huang, G. Upadhyay, Y. Ahn, M. Sakakura, G. J. Pagan-Diaz, Y. Cho, A. C. Weiss, C. Huang, J. W. Mitchell, J. Li, Y. Tan, Y. H. Deng, A. Ellis-Mohr, Z. Dou, X. Zhang, S. Kang, Q. Chen, J. V. Sweedler, S. G. Im, R. Bashir, H. J. Chung, G. Popescu, M. U. Gillette, M. Gazzola, H. Kong, Neuronal innervation regulates the secretion of neurotrophic myokines and exosomes from skeletal muscle. *Proc. Natl. Acad. Sci. U.S.A.* **121**, e2313590121 (2024).
52. C. D. Kaufman, S. C. Liu, C. Cvetkovic, C. A. Lee, G. Naseri Kouzehgarani, R. Gillette, R. Bashir, M. U. Gillette, Emergence of functional neuromuscular junctions in an engineered, multicellular spinal cord-muscle bioactuator. *APL Bioeng.* **4**, 026104 (2020).
53. O. F. Vila, S. G. M. Uzel, S. P. Ma, D. Williams, J. Pak, R. D. Kamm, G. Vunjak-Novakovic, Quantification of human neuromuscular function through optogenetics. *Theranostics* **9**, 1232–1246 (2019).
54. A. Tofangchi, A. Fan, M. T. A. Saif, Mechanism of axonal contractility in embryonic *Drosophila* motor neurons in vivo. *Biophys. J.* **111**, 1519–1527 (2016).
55. G. P. Škoro, J. R. J. Bennett, T. R. Edgecock, S. A. Gray, A. J. McFarland, C. N. Booth, K. J. Rodgers, J. J. Back, Dynamic Young's moduli of tungsten and tantalum at high temperature and stress. *J. Nucl. Mater.* **409**, 40–46 (2011).
56. P. A. Merrifield, D. W. Laird, Connexins in skeletal muscle development and disease. *Semin. Cell Dev. Biol.* **50**, 67–73 (2016).
57. T. W. Farmer, F. Buchthal, P. R. Rosenfalck, Refractory period of human muscle after the passage of a propagated action potential. *Electroencephalogr. Clin. Neurophysiol.* **12**, 455–466 (1960).
58. B. M. Carlson, "The muscular system," in *The Human Body* (Elsevier, 2019), pp. 111–136.
59. C. Cvetkovic, M. C. Ferrall-Fairbanks, E. Ko, L. Grant, H. Kong, M. O. Platt, R. Bashir, Investigating the life expectancy and proteolytic degradation of engineered skeletal muscle biological machines. *Sci. Rep.* **7**, 3775 (2017).
60. L. Grant, R. Raman, C. Cvetkovic, M. C. Ferrall-Fairbanks, G. J. Pagan-Diaz, P. Hadley, E. Ko, M. O. Platt, R. Bashir, "Long-term cryopreservation and revival of tissue-engineered skeletal muscle," in *Tissue Engineering - Part A* (Mary Ann Liebert Inc., 2019), vol. 25, pp. 1023–1036.
61. H. Wang, A. A. Svoronos, T. Boudou, M. S. Sakar, J. Y. Schell, J. R. Morgan, C. S. Chen, V. B. Shenoy, Necking and failure of constrained 3D microtissues induced by cellular tension. *Proc. Natl. Acad. Sci. U.S.A.* **110**, 20923–20928 (2013).
62. Q. Tseng, E. Duchemin-Pelletier, A. Deshiere, M. Balland, H. Guilloud, O. Filhol, M. Theŕy, Spatial organization of the extracellular matrix regulates cell-cell junction positioning. *Proc. Natl. Acad. Sci. U.S.A.* **109**, 1506–1511 (2012).
63. M. Raffel, C. E. Willert, F. Scarano, C. J. Kähler, S. T. Wereley, J. Kompenhans, *Particle Image Velocimetry A Practical Guide* (Springer, ed. 3, 2007).
64. W. Li, F. Wang, O. Sigmund, X. S. Zhang, Digital synthesis of free-form multimaterial structures for realization of arbitrary programmed mechanical responses. *Proc. Natl. Acad. Sci. U.S.A.* **119**, e2120563119 (2022).
65. J. Wang, Y. Wang, Y. Kim, T. Yu, R. Bashir, Multi-actuator light-controlled biological robots. *APL Bioeng* **6**, 036103 (2022).
66. R. Raman, C. Cvetkovic, S. G. M. Uzel, R. J. Platt, P. Sengupta, R. D. Kamm, R. Bashir, Optogenetic skeletal muscle-powered adaptive biological machines. *Proc. Natl. Acad. Sci. U.S.A.* **113**, 3497–3502 (2016).
67. C. A. Powell, B. L. Smiley, J. Mills, H. H. Vandenburgh, Mechanical stimulation improves tissue-engineered human skeletal muscle. *Am. J. Physiol. Cell Physiol.* **283**, C1557–C1565 (2002).
68. R. Mestre, T. Patiño, X. Barceló, S. Anand, A. Pérez-Jiménez, S. Sánchez, Force modulation and adaptability of 3D-bioprinted biological actuators based on skeletal muscle tissue. *Adv. Mater. Technol.* **4**, 1800631 (2019).
69. A. M. Kasper, D. C. Turner, N. R. W. Martin, A. P. Sharples, Mimicking exercise in three-dimensional bioengineered skeletal muscle to investigate cellular and molecular mechanisms of physiological adaptation. *J. Cell. Physiol.* **233**, 1985–1998 (2018).
70. K. M. Wisdom, S. L. Delp, E. Kuhl, Use it or lose it: Multiscale skeletal muscle adaptation to mechanical stimuli. *Biomech. Model. Mechanobiol.* **14**, 195–215 (2015).
71. O. F. Vila, Y. Qu, G. Vunjak-Novakovic, In vitro models of neuromuscular junctions and their potential for novel drug discovery and development. *Expert Opin. Drug Discovery* **15**, 307–317 (2020).
72. M. J. Anderson, M. W. Cohen, E. Zorychta, Effects of innervation on the distribution of acetylcholine receptors on cultured muscle cells. *J. Physiol.* **268**, 731–756 (1977).
73. Z.-P. Xie, M.-M. Poot, Initial events in the formation of neuromuscular synapse: Rapid induction of acetylcholine release from embryonic neuron. *Proc. Natl. Acad. Sci. U.S.A.* **83**, 7069–7073 (1986).
74. T. Osaki, S. G. M. Uzel, R. D. Kamm, On-chip 3D neuromuscular model for drug screening and precision medicine in neuromuscular disease. *Nat. Protoc.* **15**, 421–449 (2020).
75. S. Pak, E. Lauga, *Theoretical Models in Low-Reynolds-Number Locomotion* (Royal Society of Chemistry, 2014); www.rsc.org.
76. N. J. Derr, T. Dombrowski, C. H. Rycroft, D. Klotsa, Reciprocal swimming at intermediate Reynolds number. *J. Fluid Mech.* **952**, A8 (2022).
77. H. Liu, R. Wassersug, K. Kawshi, A computational fluid dynamics study of tadpole swimming. *J. Exp. Biol.* **199**, 1245–1260 (1996).
78. B. Jin, C. Pan, N. Xia, J. Song, H. Luo, L. Zhang, Y. Ding, Swimming of the midge larva: Principles and tricks of locomotion at intermediate Reynolds number. *Phys. Fluids* **35**, 031903 (2023).
79. S. Childress, R. Dudley, Transition from ciliary to flapping mode in a swimming mollusc: Flapping flight as a bifurcation in Re$_\omega$. *J. Fluid Mech.* **498**, 257–288 (2004).
80. A. Mancini, D. Sirabella, W. Zhang, H. Yamazaki, T. Shirao, R. S. Krauss, Regulation of myotube formation by the actin-binding factor drebrin. *Skelet. Muscle* **1**, 36 (2011).

Acknowledgments: We thank the staff at the Carl R. Woese Institute for Genomic Biology Core Facilities for training in their confocal microscope suites. **Funding:** This work was supported by the National Science Foundation Emerging Frontiers in Research and Innovation: Continuum, Compliant, and Configurable Soft Robotics Engineering grant no. 1830881 (to M.T.A.S.), the National Science Foundation Mind In Vitro grant no. 2123781 (to M.T.A.S.), the National Science Foundation Graduate Research Fellowship Program (to W.C.D.), and the Chan Zuckerberg Biohub Investigator grant (to M.T.A.S.) **Author contributions:** Conceptualization: O.A., M.T.A.S., Z.L., and W.C.D. Data curation: W.C.D., A.B., Y.K., A.C., M.W., and D.D. Formal analysis: W.C.D., A.B., and Y.K. Funding acquisition: M.T.A.S. Investigation: W.C.D., A.B., Y.K., A.C., M.W., D.D., O.A., and Z.L. Methodology: W.C.D., B.E., M.T.A.S., O.A., and Z.L. Project administration: M.T.A.S., W.C.D., and Z.L. Resources: M.T.A.S., O.A., and B.E. Software: O.A., W.C.D., A.B., and Y.K. Supervision: M.T.A.S., O.A., and Z.L. Validation: W.C.D. Visualization: W.C.D., A.B., and O.A. Writing—original draft: W.C.D., M.T.A.S., and M.S.H.J. Writing—review and editing: W.C.D., M.T.A.S., O.A., and M.S.H.J. **Competing interests:** The authors declare that they have no competing interests. **Data and materials availability:** All data needed to evaluate the conclusions in the paper are present in the paper and/or the Supplementary Materials.

Submitted 28 November 2024
Accepted 16 May 2025
Published 16 July 2025
10.1126/sciadv.adu8634